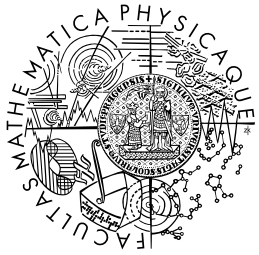

FACULTY
OF MATHEMATICS
AND PHYSICS
Charles University

MASTER THESIS

Tomáš Maleček

Substrate controlled physical properties of magnetic oxides thin films for spintronic applications

Institute of Physics of Charles University

Supervisor of the master thesis: RNDr. Martin Veis, Ph.D.
Study programme: Physics
Study branch: Optics and Optoelectronics

Prague 2022

I declare that I carried out this master thesis independently, and only with the cited sources, literature and other professional sources. It has not been used to obtain another or the same degree.

I understand that my work relates to the rights and obligations under the Act No. 121/2000 Sb., the Copyright Act, as amended, in particular the fact that the Charles University has the right to conclude a license agreement on the use of this work as a school work pursuant to Section 60 subsection 1 of the Copyright Act.

In ..... date ....

Author's signature

This thesis is dedicated to you, the reader.

Title: Substrate controlled physical properties of magnetic oxides thin films for spintronic applications

Author: Tomáš Maleček

Institute: Institute of Physics of Charles University

Supervisor: RNDr. Martin Veis, Ph.D., Institute of Physics of Charles University

Abstract: As conventional electronics approaches its fundamental limits, new paradigms are required. Integration of new spintronic materials with current silicon technology shows great promise. This thesis demonstrates the possibility of growing textured stress-free $La_{2/3}Sr_{1/3}MnO_3$ (LSMO) thin films on silicon with properties comparable to epitaxially grown layers on $SrTiO_3$ (STO). Growth of LSMO is achieved by a two-dimensional nanosheet (NS) seed layer of $Ca_2Nb_3O_{10}$ inducing epitaxial stabilization of LSMO films. Samples of LSMO on NS/Si, prepared by pulsed laser deposition, have been shown to have lower magnetization than samples of LSMO on STO yet also possess a higher Curie temperature by more than 10 K. Spectral dependence of the full permittivity tensor was calculated from optical and magneto-optical measurements. Spectra of the off-diagonal element have been fitted with three diamagnetic transitions located around 1.9, 2.9 and 3.5 eV for samples on NS/Si as well as for samples on STO. Similarities between the samples open the possibility of integration of LSMO into silicon technology using NS. Temperature-dependent optical and magneto-optical properties of a sample of LSMO on STO have been evaluated.

Keywords: magneto-optical Kerr effect, permittivity tensor, epitaxial strain, nanosheets, pulsed laser deposition, LSMO

Contents

Introduction

This thesis is devoted to the growth and study of textured $La_{2/3}Sr_{1/3}MnO_3$ (LSMO) thin films on a silicon substrate using a nanosheet seed layer. Epitaxially grown thin films of LSMO atop $SrTiO_3$ (STO) and $BaTiO_3$ (BTO) have been prepared for comparison.

The half-metallic ferromagnetic LSMO is an auspicious candidate for application in technological devices such as sensors, data storage media, and detectors. That is due to its unique combination of physical properties. Almost total spin polarization [1] coupled with its ferromagnetic nature could have wide uses in spin electronics. LSMO also exhibits colossal magnetoresistance (CMR) [2] and a high Curie temperature ($T_C^{Bulk} \approx 370$ K [3]).

Ferromagnetic ordering of LSMO has been explained by C. Zenner [4] using a double-exchange (DE) interaction, an e_g electron transfer between the Mn^{3+} and Mn^{4+} ions via an O^{2-} $2p$ state. The probability of this transfer is dependent on the Mn^{3+} - O^{2-} - Mn^{4+} geometry and hence on the epitaxial strain.

In order to easily integrate LSMO devices into current electronics, they have to be compatible with current silicon technology. So far, this integration has been done using an STO buffer layer [5]. In this thesis, we introduce a different approach. By chemical deposition of a single nanosheet layer of $Ca_2Nb_3O_{10}$ on silicon, we are able to grow a strain-free thin film of LSMO by pulsed laser deposition.

This thesis is organized into five chapters. The first three chapters of the thesis are devoted to the theory and experimental methods utilized within it. The fourth chapter introduces the investigated samples. Following are the experimental results in chapter five describing the growth of the thin films by pulsed laser deposition, their evaluation by X-ray diffraction, atomic force microscopy, and magnetometry measurements. Finally, the full permittivity tensor of the thin films is numerically calculated from optical and magneto-optical measurements and fitted with magneto-optical transitions giving insight into the electronic structure of the samples. Additionally, temperature-dependent optical and magneto-optical setups are constructed, and temperature-dependent measurements are carried out on an LSMO/STO sample.

1. Polarization of light and magneto-optical effects

This chapter introduces the basic theory of light polarization and describes its propagation using Jones calculus. Furthermore, magneto-optical observables are defined and the permittivity tensor along with its symmetries is introduced. The chapter concludes with Yeh formalism describing the propagation of light through layered anisotropic media.

1.1 The polarization ellipse

Polarization is a property of transverse waves. In classical physics, light can be described as a transverse plane wave, and hence we can define its polarization state. The polarization state of light describes the oscillation of the electric field vector $\boldsymbol{E}$.

Let us assume a plane wave solution to Maxwell's equations traveling along the $\boldsymbol{z}$ axis. A harmonic monochromatic plane wave can then be described as a superposition of independent oscillations along Cartesian axes as

$$E_x(z,t) = E_{0x}\,\cos(\omega t - k_z z + \delta_x)\,, \tag{1.1}$$

$$E_y(z,t) = E_{0y}\,\cos(\omega t - k_z z + \delta_y)\,, \tag{1.2}$$

$$E_z(z,t) = 0\,, \tag{1.3}$$

where E_{0x} and E_{0y} are amplitudes of the oscillations, δ_x and δ_y are phase offsets, ω represents angular frequency and k_z represents the only non-zero component of the wave vector. It can be shown [6] that in the general case, the electric field vector $\boldsymbol{E}$ traces an ellipse in the plane perpendicular to the wave vector (see Fig. 1.1).

The polarization ellipse (i.e., the polarization state) is defined by four parameters. They are as follows:

- The *amplitude* E_0 - overall wave amplitude given by $E_0 = \sqrt{a^2 + b^2} = \sqrt{E_{0x}^2 + E_{0y}^2}$. It relates to light intensity as $I = E_0^2 = a^2 + b^2$.
- The *ellipticity* e - ratio of the semi-minor axis b to the semi-major axis a. The sign of ellipticity represents the handedness of polarization. In this thesis we assign positive values to right-handed polarization. An associated parameter is the *ellipticity angle* ϵ defined by $tan\epsilon = e$.
- The *azimuth* θ - an oriented angle between the positive semi-axis $\boldsymbol{x}$ and the major axis of the ellipse.
- The *absolute phase* δ_0 - angle between the initial state of the electric field vector $\boldsymbol{E}(t = 0)$ and the $\boldsymbol{x}$ axis.

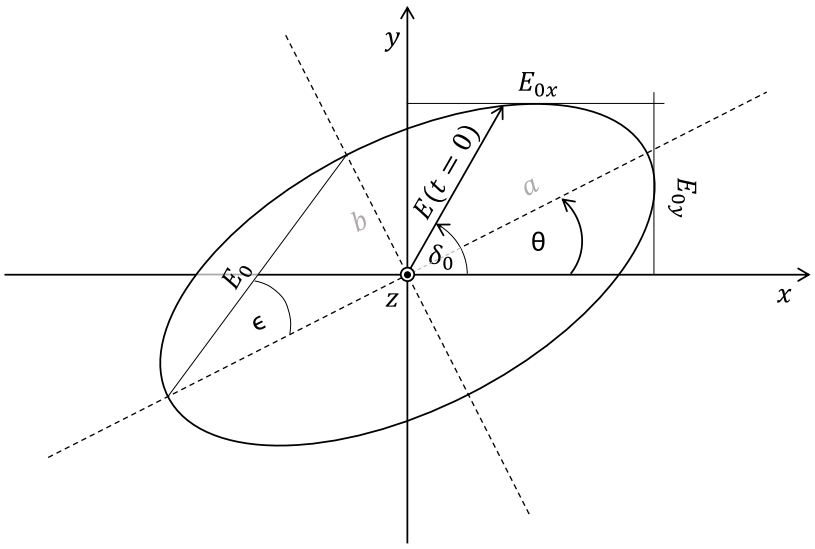

Figure 1.1: The polarization ellipse when looking against the propagation of light.

When describing the polarization state we will generally restrict ourselves to the ellipticity (or ellipticity angle) and the azimuth. The amplitude carries information about the absolute intensity of light which is often of no interest to us. Similarly, the absolute phase provides only information about the initial state, which bears little relevance to this thesis.

The polarization state of light with zero ellipticity angle is referred to as linear polarization. The polarization state of light with an ellipticity angle equal to $\frac{\pi}{4}$ is referred to as right circular polarization (RCP), and a polarization state with the opposite ellipticity angle $-\frac{\pi}{4}$ is referred to as left circular polarization (LCP).

1.1.1 Complex polarization parameter

Equations (1.1) and (1.2) can be rewritten using complex notation as

$$E_x(z,t) = Re\{E_{0x}e^{i(\omega t - kz + \delta_x)}\} = Re\{A_x e^{i(\omega t - kz)}\}\,, \tag{1.4}$$

$$E_y(z,t) = Re\{E_{0y}e^{i(\omega t - kz + \delta_y)}\} = Re\{A_y e^{i(\omega t - kz)}\}\,, \tag{1.5}$$

where A_x and A_y are complex amplitudes. The complex polarization parameter is then defined as

$$\chi \equiv \frac{A_y}{A_x} = \tan\alpha e^{i\delta}\,. \tag{1.6}$$

The complex polarization parameter χ is introduced as an alternative to the previously defined two real parameters (azimuth and ellipticity angle). The equation (1.6) also defines two new real parameters α and δ which obey

$$\tan\alpha = \frac{E_{0y}}{E_{0x}}\,, \qquad \delta = \delta_y - \delta_x\,. \tag{1.7}$$

The complex polarization parameter relates to the azimuth and the ellipticity angle through

$$\chi = \frac{\tan\theta + i\tan\epsilon}{1 - i\tan\theta\tan\epsilon}\,. \tag{1.8}$$

If the angles θ and ϵ are small, their tangent functions can be approximated by their arguments. Because of the small-angle assumption, the second term in the denominator approaches zero. Thus for small angles of azimuth and ellipticity, it holds true that

$$\chi \approx \theta + i\epsilon\,. \tag{1.9}$$

1.2 Jones calculus

Jones calculus is introduced in order to effectively model the propagation of light polarization through an optical system. It is a simple yet powerful formalism accurately describing fully polarized light, i.e., light consisting of only one polarization state. Light is represented by Jones vectors and optical elements are represented by Jones matrices.

1.2.1 Jones vector

Jones vector is defined as

$$\boldsymbol{J} = \begin{bmatrix} E_{0x}e^{i\delta_x} \\ E_{0y}e^{i\delta_y} \end{bmatrix} = \begin{bmatrix} A_x \\ A_y \end{bmatrix}\,, \tag{1.10}$$

and carries the complete polarization information. As discussed earlier in this chapter, the amplitude and the absolute phase of light are redundant, and thus the normalized Jones vector can be written as

$$\boldsymbol{J} = \begin{bmatrix} \cos\alpha \\ \sin\alpha\ e^{i\delta} \end{bmatrix}\,. \tag{1.11}$$

The Jones vector can be expressed in terms of any basis. The most common are the Cartesian and the circular basis. The Cartesian basis represents light in terms of linear polarization along the $\boldsymbol{x}$ and $\boldsymbol{y}$ axes. The circular basis uses as base vectors circularly polarized light with one vector representing left circular polarization and the other right circular polarization.

1.2.2 Jones matrix

Optical elements in Jones formalism are represented by matrices. We differentiate between transmission and reflection elements and their matrices. Let us first consider the transmission of light through an optical element. The incident Cartesian coordinate system $\boldsymbol{S}^{(I)}$ (see Fig. 1.2(a)) is oriented so that the $\boldsymbol{z}^{(I)}$ axis coincides with the wave vector, the $\boldsymbol{y}^{(I)}$ axis is parallel to the plane of incidence

and the $\boldsymbol{x}^{(I)}$ axis is perpendicular to the plane of incidence. Light linearly polarized parallel to the plane of incidence is often called p-polarized (*parallel*). Light with a linear polarization perpendicular to the plane of incidence is said to be s-polarized (from German *senkrecht* - perpendicular). The Cartesian coordinate system after transmission $\boldsymbol{S}^{(T)}$ is defined analogously.

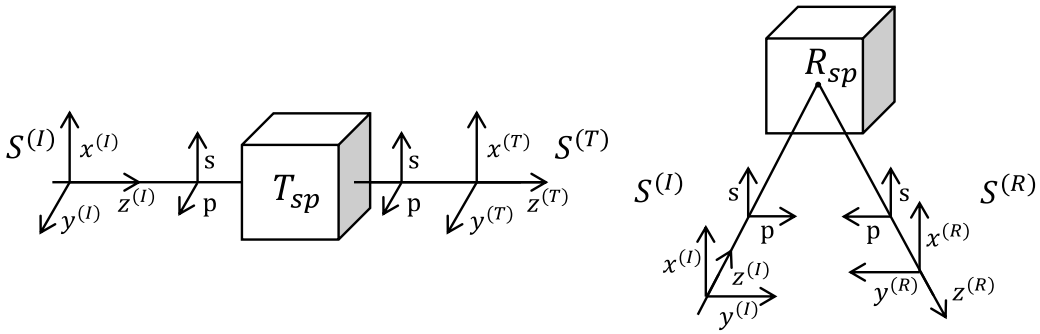

(a) (b)

Figure 1.2: Cartesian coordinate systems for the transmission (a) and reflection (b) of light.

Let us now have an incident light wave on an optical element represented by Jones vector $\boldsymbol{J}^{(I)}$ and a transmitted light wave represented by $\boldsymbol{J}^{(T)}$. The Jones transmission matrix $\boldsymbol{T}_{sp}$ is then defined by the relation

$$\boldsymbol{J}^{(T)} = \boldsymbol{T}_{sp}\, \boldsymbol{J}^{(I)}\,. \tag{1.12}$$

The Jones transmission matrix can be written in terms of its components as

$$\boldsymbol{T}_{sp} = \begin{bmatrix} t_{ss} & t_{sp} \\ t_{ps} & t_{pp} \end{bmatrix}\,. \tag{1.13}$$

Using the definition of Jones matrix (1.12) and the definition of Jones vector (1.10) we can write the relations between the matrix elements and the complex amplitudes of the light wave. The relations in terms of s,p-polarizations are

$$t_{ss} = \left(\frac{A_s^{(T)}}{A_s^{(I)}}\right)_{A_p^{(I)}=0}\,, \tag{1.14}$$

$$t_{sp} = \left(\frac{A_s^{(T)}}{A_p^{(I)}}\right)_{A_s^{(I)}=0}\,, \tag{1.15}$$

$$t_{ps} = \left(\frac{A_p^{(T)}}{A_s^{(I)}}\right)_{A_p^{(I)}=0}\,, \tag{1.16}$$

$$t_{pp} = \left(\frac{A_p^{(T)}}{A_p^{(I)}}\right)_{A_s^{(I)}=0}\,. \tag{1.17}$$

To describe the reflection matrix of an element, we define two Cartesian coordinate systems $\boldsymbol{S}^{(I)}$ and $\boldsymbol{S}^{(R)}$ similarly to the transmission case and according

to Fig. 1.2(b). Let us also have an incident light wave represented by $\boldsymbol{J}^{(I)}$ and a reflected light wave represented by $\boldsymbol{J}^{(R)}$. The Jones reflection matrix is then defined as

$$\boldsymbol{J}^{(R)} = \boldsymbol{R}_{sp}\, \boldsymbol{J}^{(I)}\,. \tag{1.18}$$

The reflection matrix written in terms of its components is

$$\boldsymbol{R}_{sp} = \begin{bmatrix} r_{ss} & r_{sp} \\ r_{ps} & r_{pp} \end{bmatrix}\,, \tag{1.19}$$

and the matrix elements of the Jones reflection matrix are then given by

$$r_{ss} = \left(\frac{A_s^{(R)}}{A_s^{(I)}}\right)_{A_p^{(I)}=0}\,, \tag{1.20}$$

$$r_{sp} = \left(\frac{A_s^{(R)}}{A_p^{(I)}}\right)_{A_s^{(I)}=0}\,, \tag{1.21}$$

$$r_{ps} = \left(\frac{A_p^{(R)}}{A_s^{(I)}}\right)_{A_p^{(I)}=0}\,, \tag{1.22}$$

$$r_{pp} = \left(\frac{A_p^{(R)}}{A_p^{(I)}}\right)_{A_s^{(I)}=0}\,. \tag{1.23}$$

We have defined the interaction of polarized light with an optical element. To model the propagation of polarization through the entire system, we have only to multiply the Jones vector of the incident light wave by the matrix of each element in the order with which they appear in the system. Each matrix element has to be represented in the same basis. The process of switching bases in Jones formalism is identical to bases switching in linear algebra and can be found in [7].

1.3 Magneto-optical Kerr effect

Magneto-optical Kerr effect (MOKE) is a measure of magnetically induced optical anisotropy in a sample. The magneto-optical Kerr effect is measured in reflection geometry. The magnetically introduced anisotropy measured in transmission geometry is called the magneto-optical Faraday effect.

Let us consider an optically isotropic sample and a basis of s and p-polarizations (as per Fig. 1.2(b)). In such a coordinate system, the Jones reflection matrix of the sample will be diagonal. That is because the s and p-polarizations do not mix upon reflection. However, suppose our sample is ferromagnetic (as all samples in this thesis are) and is exposed to an external magnetic field. Then the subsequent magnetization of the sample induces optical anisotropy. This leads to a sample reflection matrix that is no longer diagonal. For an incident s-polarised wave we define the *complex magneto-optical Kerr angle* Φ_{Ks} as the negative ratio of the off-diagonal and diagonal elements of the reflection matrix. Using (1.20) and (1.22) we can express that ratio for an incident s-polarised wave as

$$\Phi_{Ks} \equiv -\frac{r_{ps}}{r_{ss}} = -\left(\frac{\frac{A_p^{(R)}}{A_s^{(I)}}}{\frac{A_s^{(R)}}{A_s^{(I)}}}\right)_{A_p^{(I)}=0} = -\left(\frac{A_p^{(R)}}{A_s^{(R)}}\right)_{A_p^{(I)}=0} = -\chi_s^{(R)}\,. \tag{1.24}$$

From the definition of the complex polarization parameter (1.6) we see that it is equal to the negative complex magneto-optical (MO) angle. Assuming that the azimuth $\theta_s^{(R)}$ and the ellipticity angle $\epsilon_s^{(R)}$ after reflection are small (i.e., the induced anisotropy is small), we can use the approximation (1.9) to write the complex polarization parameter as

$$\chi_s^{(R)} \approx \theta_s^{(R)} + i\epsilon_s^{(R)}\,. \tag{1.25}$$

Using this relation we can introduce real magneto-optical angles *Kerr rotation* θ_{Ks} and *Kerr ellipticity* ϵ_{Ks} for an incident s-polarized wave as

$$\theta_{Ks} \equiv -\theta_s^{(R)}\,, \tag{1.26}$$

$$\epsilon_{Ks} \equiv \epsilon_s^{(R)}\,, \tag{1.27}$$

$$\Phi_{Ks} \approx \theta_{Ks} - i\epsilon_{Ks}\,. \tag{1.28}$$

For the case of incident p-polarization the positive value of the ratio of the matrix elements defines the *complex magneto-optical angle* Φ_{Kp}. Using (1.21) and (1.23) we can show that

$$\Phi_{Kp} \equiv \frac{r_{sp}}{r_{pp}} = \left(\frac{\frac{A_s^{(R)}}{A_p^{(I)}}}{\frac{A_p^{(R)}}{A_p^{(I)}}}\right)_{A_s^{(I)}=0} = \left(\frac{A_s^{(R)}}{A_p^{(R)}}\right)_{A_s^{(I)}=0} = (\chi_p^{(R)})^{-1}\,. \tag{1.29}$$

The azimuth $\theta_p^{(R)}$ no longer satisfies the small-angle assumption as it is close to $\pi/2$. However, it can be shown [6] that if the azimuth is sufficiently close to $\pi/2$ (which for magnetically induced anisotropy generally holds true for incident p-polarization), the complex polarization parameter can be approximated as

$$(\chi_p^{(R)})^{-1} \approx \frac{\pi}{2} - \theta_p^{(R)} - i\epsilon_p^{(R)}\,. \tag{1.30}$$

We can then define the real magneto-optical angles *Kerr rotation* θ_{Kp} and *Kerr ellipticity* ϵ_{Kp} for an incident p-polarised wave as

$$\theta_{Kp} \equiv \frac{\pi}{2} - \theta_p^{(R)}\,, \tag{1.31}$$

$$\epsilon_{Kp} \equiv \epsilon_p^{(R)}\,, \tag{1.32}$$

$$\Phi_{Kp} \approx \theta_{Kp} - i\epsilon_{Kp}\,. \tag{1.33}$$

In the case of normal incidence the distinction between s and p-polarizations can not be made. From the symmetry of the problem the off-diagonal elements of the Jones reflection matrix of the sample must be equal to one another. The diagonal elements of the reflection matrix are equal in magnitude but have opposite signs due to the change of the coordinate system (see Fig. 1.2(b)). It then follows that for normal incidence

$$\Phi_K \equiv \Phi_{Ks} = \Phi_{Kp} \approx \theta_K - i\epsilon_K \,. \tag{1.34}$$

1.4 Permittivity tensor

The permittivity tensor is a material property essential for modelling light interaction with any media. It carries information about the interaction of light with the investigated system and can also be used to draw conclusions about the underlying phenomena. In general, permittivity is a second-order tensor

$$\boldsymbol{\varepsilon} = \begin{bmatrix} \varepsilon_{xx} & \varepsilon_{xy} & \varepsilon_{xz} \\ \varepsilon_{yx} & \varepsilon_{yy} & \varepsilon_{yz} \\ \varepsilon_{zx} & \varepsilon_{zy} & \varepsilon_{zz} \end{bmatrix} . \tag{1.35}$$

For an optically isotropic sample permittivity is a scalar. If we introduce a magnetic field into the system, the subsequent magnetization of the material $\boldsymbol{M} = (M_x, M_y, M_z)$ induces anisotropy, and therefore influences the permittivity tensor. The influence, typically small, can be considered a perturbation. Thus we can define its MacLaurin series and approximate permittivity by

$$\varepsilon_{ij} \approx \varepsilon_{ij}(0) + \left(\frac{\partial \varepsilon_{ij}}{\partial M_k} \right)_{M=0} M_k \,, \tag{1.36}$$

where the indices *i,j,k* represent any of the indices of the Cartesian axes. We have restricted ourselves to the first order of the perturbation as the second-order term is cancelled out by the measurement technique (see Section 3.6), and the following terms have a negligible impact.

The permittivity tensor has to abide by the system symmetry. For this reason we introduce three standard geometries used for magneto-optical measurements. These geometries lead to the simplification of the permittivity tensor. The geometry used thought-out this thesis is the *polar geometry* (see Fig. 1.3(a)) in which the magnetization is perpendicular to the sample surface. The permittivity tensor in this geometry has to be invariant with respect to rotation around the $\boldsymbol{z}$ axis. Permittivity then takes the form

$$\boldsymbol{\varepsilon}_p = \begin{bmatrix} \varepsilon_{xx} & \varepsilon_{xy} & 0 \\ -\varepsilon_{xy} & \varepsilon_{xx} & 0 \\ 0 & 0 & \varepsilon_{zz} \end{bmatrix} . \tag{1.37}$$

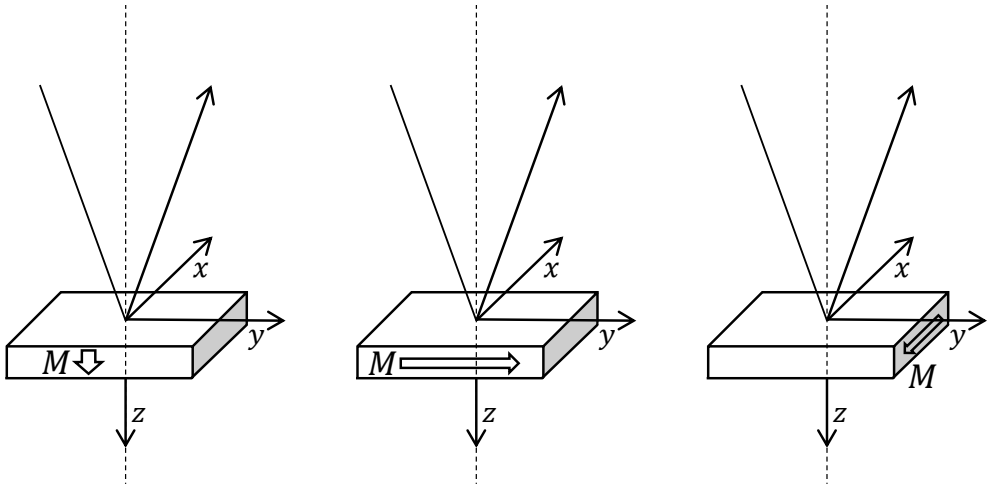

(a) (b) (c)

Figure 1.3: Definitions of polar (a), longitudinal (b) and transversal (c) geometries for MOKE measurements for a magnetized sample.

Due to the restriction to linear magneto-optical effects it can be shown [8] that $\varepsilon_{xx} \approx \varepsilon_{zz}$ for all geometries. The permittivity tensor is then conventionally written as -

$$\boldsymbol{\varepsilon}_p = \begin{bmatrix} \varepsilon_1 & i\varepsilon_2 & 0 \\ -i\varepsilon_2 & \varepsilon_1 & 0 \\ 0 & 0 & \varepsilon_1 \end{bmatrix} . \tag{1.38}$$

Second is the *longitudinal geometry* that can be seen in Fig. 1.3(b). The magnetization of the material is in-plane of the sample and also lies within the plane of incidence. The permittivity tensor for the longitudinal geometry is

$$\boldsymbol{\varepsilon}_l = \begin{bmatrix} \varepsilon_1 & 0 & i\varepsilon_2 \\ 0 & \varepsilon_1 & 0 \\ -i\varepsilon_2 & 0 & \varepsilon_1 \end{bmatrix} . \tag{1.39}$$

Lastly the *transversal geometry* is defined by in-plane magnetization that is perpendicular to the plane of incidence (see Fig. 1.3(c)). Its permittivity tensor takes the form

$$\boldsymbol{\varepsilon}_t = \begin{bmatrix} \varepsilon_1 & 0 & 0 \\ 0 & \varepsilon_1 & i\varepsilon_2 \\ 0 & -i\varepsilon_2 & \varepsilon_1 \end{bmatrix} . \tag{1.40}$$

1.5 Magneto-optical transitions

A semiclassical microscopic approach allows for the description of spectral features in the off-diagonal element of the permittivity tensor. Analysis of the off-diagonal element of the permittivity tensor gives insight into the electronic structure of the material. This is due to close ties between magnetism, optics and the electronic structure of a material. Spectral features result from different absorption of LCP and RCP owing to a spin-orbit splitting of degenerated states. Due to the selection rules, transitions between the split states are exclusive to one circular polarization state [9].

For simplicity, only splitting of one state at a time is considered. Thus we recognize two types of MO active transitions. Type I single (paramagnetic) transition results from the splitting of the ground state (see Fig. 1.4). The spectral dependence of the off-diagonal element of the permittivity tensor for a paramagnetic transition (taken from Ref. [10]) is

$$\varepsilon_2(\omega) = 2\Gamma(\varepsilon_2'')_{max}\frac{\omega(\omega^2 - E_0^2 + \Gamma^2) - i\Gamma(\omega^2 + E_0^2 - \Gamma^2)}{(\omega^2 - E_0^2 - \Gamma^2)^2 + 4\Gamma^2\omega^2}, \tag{1.41}$$

where Γ is the half-width at half-maximum, $(\varepsilon_2'')_{max}$ is the maximum amplitude of the imaginary part of the off-diagonal element of the permittivity tensor and E_0 is the center energy of the transition.

Type II double (diamagnetic) transition originates from the splitting of the excited states, and its spectral dependency of the off-diagonal element of the permittivity tensor (taken from Ref. [10]) is

$$\varepsilon_2(\omega) = \Gamma^2(\varepsilon_2')_{max}\frac{(\omega - E_0)^2 - \Gamma^2 + 2i\Gamma(\omega - E_0)}{[(\omega - E_0)^2 + \Gamma^2]^2}. \tag{1.42}$$

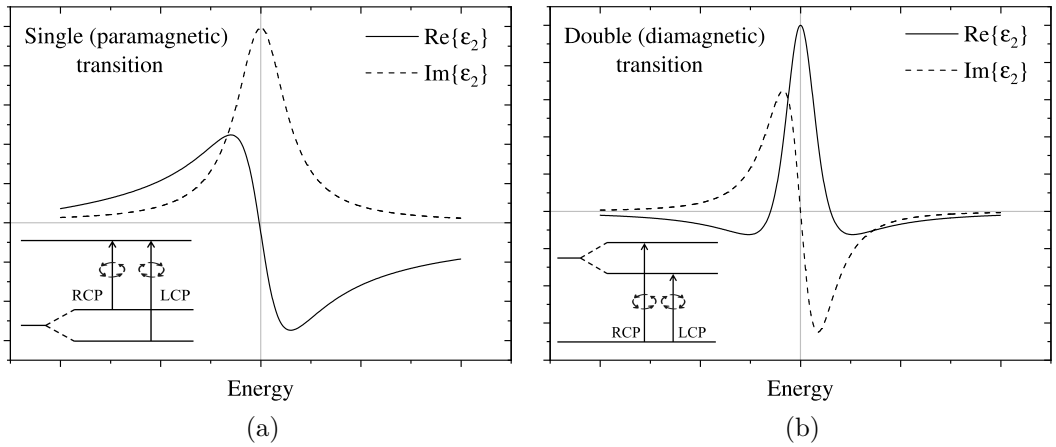

Figure 1.4: Spectral shapes of magneto-optical transitions. (a) Single (paramagnetic) transition originating from the splitting of the ground state. (b) Double (diamagnetic) transition originating from the splitting of the excited state.

1.6 Yeh formalism

The Yeh formalism describes the propagation of light through layered anisotropic media. It has been greatly advanced by prof. Višňovský [8] most notably by expanding it to magneto-optical effects. Analytical calculations of the magneto-optical response of a sample can be carried out using this formalism. Utilizing the knowledge of the permittivity tensor of each of the sample layers, we can calculate the magneto-optical Kerr effect.

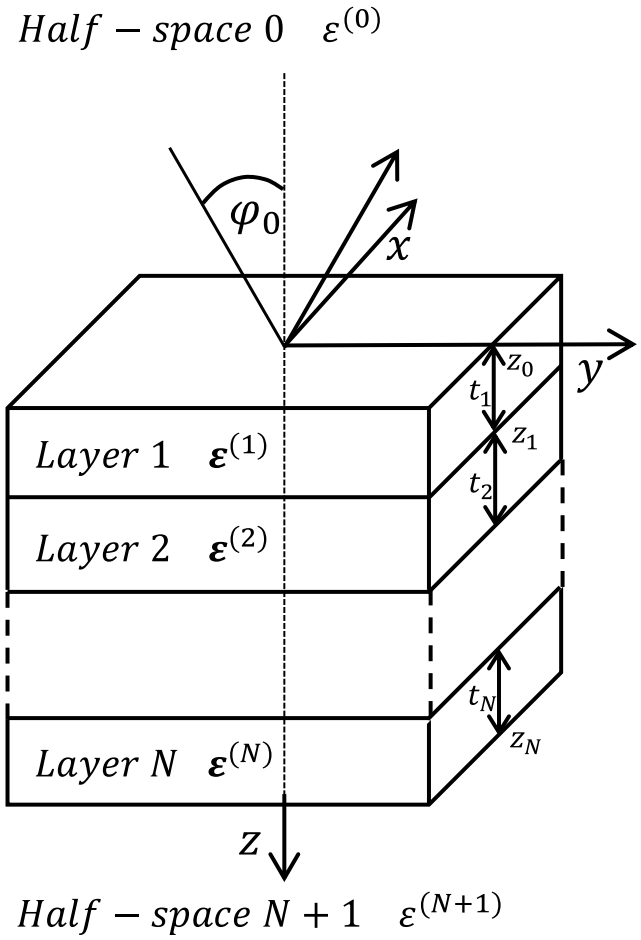

Figure 1.5: Multilayer structure consisting of N anisotropic layers, with corresponding tensor permittivities $\boldsymbol{\varepsilon}^{(n)}$, thicknesses t_n and interface coordinates z_n. The investigated structure is surrounded by two optically isotropic half-spaces with corresponding scalar permittivities $\varepsilon^{(0)}$ and $\varepsilon^{(N+1)}$.

Let us now consider a layered sample structure (see Fig. 1.5). The structure consists of N layers that are parallel to one another and perpendicular to the $\boldsymbol{z}$ axis. The structure is surrounded by two isotropic half-spaces. The half-space *N+1* is an idealization of the substrate. Each layer has a corresponding tensor permittivity $\boldsymbol{\varepsilon}^{(n)}$ and thickness t_n. The two isotropic half-spaces have scalar permittivities $\varepsilon^{(0)}$ and $\varepsilon^{(N+1)}$ respectively. The interfaces between the layers are defined by their z_n coordinates on the $\boldsymbol{z}$ axis. For an incident monochromatic plane wave we define a right-handed Cartesian coordinate system such that the $\boldsymbol{x}$ axis is perpendicular to the plane of incidence. The angle of incidence is φ_0.

In order to model the response of the sample we need to solve the wave equation in all layers of the structure. Let the layers be ferromagnetic (i.e., optically anisotropic) without any free current or charge. We shall also assume the permeability tensor $\boldsymbol{\mu}$ to be a scalar and equal to one. This has been shown in literature to hold true for optical frequencies [11, 12]. Using Maxwell's equations and constitutive relations, the wave equation for the n-th layer can then be written as

$$\Delta \boldsymbol{E}^{(n)} - \varepsilon_0 \mu_0 \boldsymbol{\varepsilon}^{(n)} \frac{\partial^2 \boldsymbol{E}^{(n)}}{\partial t^2} - \nabla(\nabla \cdot \boldsymbol{E}^{(n)}) = 0\,, \tag{1.43}$$

where c is the speed of light in a vacuum. The solution to the wave equation can be written in the form of a plane wave as

$$\boldsymbol{E}^{(n)} = \boldsymbol{E}_0^{(n)} e^{i(\omega t - \boldsymbol{k}^{(n)} \cdot \boldsymbol{r})}\,. \tag{1.44}$$

We further introduce a reduced wave vector $\boldsymbol{N}$ as the wave vector for a given medium divided by the magnitude of the wave vector in a vacuum. That can also be written in the form of

$$\boldsymbol{N}^{(n)} = \frac{c}{\omega} \boldsymbol{k}^{(n)}\,. \tag{1.45}$$

The N_x component in our coordinate system is equal to zero in all layers. For the N_y component, it follows from Snell's law that it is constant across all layers and is equal to

$$N_y = N_0 \sin \varphi_0\,, \tag{1.46}$$

We can substitute the plane wave solution (1.44) to the wave equation (1.43) and rewrite it in matrix form using the reduced wave vector as

$$\begin{bmatrix} \varepsilon_{xx}^{(n)} - N_y^2 - (N_z^{(n)})^2 & \varepsilon_{xy}^{(n)} & \varepsilon_{xz}^{(n)} \\ \varepsilon_{yx}^{(n)} & \varepsilon_{yy}^{(n)} - (N_z^{(n)})^2 & \varepsilon_{yz}^{(n)} + N_y N_z^{(n)} \\ \varepsilon_{zx}^{(n)} & \varepsilon_{zy}^{(n)} + N_y N_z^{(n)} & \varepsilon_{zz}^{(n)} - N_y^2 \end{bmatrix} \begin{bmatrix} E_{0x}^{(n)} \\ E_{0y}^{(n)} \\ E_{0z}^{(n)} \end{bmatrix} = 0\,. \tag{1.47}$$

The non-trivial solution to the above equation exists if the determinant of the matrix is equal to zero. If we write the characteristic equation of the matrix, we can find its four eigenvalues $N_{zj}^{(n)}$ and their corresponding eigenvectors $\boldsymbol{e}_j^{(n)}$. The eigenvectors and eigenvalues describe the eigenmodes of light waves in a given layer n. The general solution to the equation (1.47) is then

$$\boldsymbol{E}^{(n)} = \sum_{j=1}^{4} E_{0j}^{(n)}(z_n) \boldsymbol{e}_j^{(n)} e^{i\left\{\omega t - \frac{\omega}{c}\left[N_y y + N_{zj}^{(n)}(z - z_n)\right]\right\}}\,. \tag{1.48}$$

The magnetic field of a plane wave can be calculated from Maxwell's equations as

$$\boldsymbol{B} = \frac{1}{c}\boldsymbol{N} \times \boldsymbol{E}\,, \tag{1.49}$$

therefore, the magnetic field eigenvectors $\boldsymbol{b}_j^{(n)}$ are

$$\boldsymbol{b}_j^{(n)} = \boldsymbol{N}_j^{(n)} \times \boldsymbol{e}_j^{(n)}\,, \tag{1.50}$$

and the magnetic field of the plane wave in terms of its eigenmodes is then given by

$$\boldsymbol{B}^{(n)} = \frac{1}{c}\sum_{j=1}^{4} E_{0j}^{(n)}(z_n)\boldsymbol{b}_j^{(n)} e^{i\left\{\omega t - \frac{\omega}{c}\left[N_y y + N_{zj}^{(n)}(z-z_n)\right]\right\}}\,. \tag{1.51}$$

The solutions of the wave equations in each layer have to be tied together via boundary conditions. At the interface of two layers without free current and charge the tangential components of the electric field vector and the magnetic field vector have to be continuous. This requirement can be expressed mathematically as

$$\sum_{j=1}^{4} E_{0j}^{(n-1)}(z_{n-1})\boldsymbol{e}_j^{(n-1)} \cdot \boldsymbol{x} = \sum_{j=1}^{4} E_{0j}^{(n)}(z_n)\boldsymbol{e}_j^{(n)} \cdot \boldsymbol{x} e^{i\frac{\omega}{c}N_{zj}^{(n)}t_n}\,, \tag{1.52}$$

$$\sum_{j=1}^{4} E_{0j}^{(n-1)}(z_{n-1})\boldsymbol{b}_j^{(n-1)} \cdot \boldsymbol{y} = \sum_{j=1}^{4} E_{0j}^{(n)}(z_n)\boldsymbol{b}_j^{(n)} \cdot \boldsymbol{y} e^{i\frac{\omega}{c}N_{zj}^{(n)}t_n}\,, \tag{1.53}$$

$$\sum_{j=1}^{4} E_{0j}^{(n-1)}(z_{n-1})\boldsymbol{e}_j^{(n-1)} \cdot \boldsymbol{y} = \sum_{j=1}^{4} E_{0j}^{(n)}(z_n)\boldsymbol{e}_j^{(n)} \cdot \boldsymbol{y} e^{i\frac{\omega}{c}N_{zj}^{(n)}t_n}\,, \tag{1.54}$$

$$\sum_{j=1}^{4} E_{0j}^{(n-1)}(z_{n-1})\boldsymbol{b}_j^{(n-1)} \cdot \boldsymbol{x} = \sum_{j=1}^{4} E_{0j}^{(n)}(z_n)\boldsymbol{b}_j^{(n)} \cdot \boldsymbol{x} e^{i\frac{\omega}{c}N_{zj}^{(n)}t_n}\,. \tag{1.55}$$

The Yeh formalism utilizes matrices for the description of propagation of light through layered anisotropic media. The above equations can be formulated in matrix form as

$$\boldsymbol{D}^{(n-1)}\boldsymbol{E}_0^{(n-1)}(z_{n-1}) = \boldsymbol{D}^{(n)}\boldsymbol{P}^{(n)}\boldsymbol{E}_0^{(n)}(z_n)\,, \tag{1.56}$$

where the dynamical $\boldsymbol{D}^{(n)}$ and propagation $\boldsymbol{P}^{(n)}$ matrices are introduced. The dynamical matrix represents the propagation of light across the interface between two layers and is defined by

$$\boldsymbol{D}^{(n)} = \begin{bmatrix} \boldsymbol{e}_1^{(n)} \cdot \boldsymbol{x} & \boldsymbol{e}_2^{(n)} \cdot \boldsymbol{x} & \boldsymbol{e}_3^{(n)} \cdot \boldsymbol{x} & \boldsymbol{e}_4^{(n)} \cdot \boldsymbol{x} \\ \boldsymbol{b}_1^{(n)} \cdot \boldsymbol{y} & \boldsymbol{b}_2^{(n)} \cdot \boldsymbol{y} & \boldsymbol{b}_3^{(n)} \cdot \boldsymbol{y} & \boldsymbol{b}_4^{(n)} \cdot \boldsymbol{y} \\ \boldsymbol{e}_1^{(n)} \cdot \boldsymbol{y} & \boldsymbol{e}_2^{(n)} \cdot \boldsymbol{y} & \boldsymbol{e}_3^{(n)} \cdot \boldsymbol{y} & \boldsymbol{e}_4^{(n)} \cdot \boldsymbol{y} \\ \boldsymbol{b}_1^{(n)} \cdot \boldsymbol{x} & \boldsymbol{b}_2^{(n)} \cdot \boldsymbol{x} & \boldsymbol{b}_3^{(n)} \cdot \boldsymbol{x} & \boldsymbol{b}_4^{(n)} \cdot \boldsymbol{x} \end{bmatrix}\,. \tag{1.57}$$

The propagation matrix describes the propagation of the light wave through a given layer and is defined as

$$\boldsymbol{P}^{(n)} = \begin{bmatrix} e^{i\frac{\omega}{c}N_{z1}^{(n)}t_n} & 0 & 0 & 0 \\ 0 & e^{i\frac{\omega}{c}N_{z2}^{(n)}t_n} & 0 & 0 \\ 0 & 0 & e^{i\frac{\omega}{c}N_{z3}^{(n)}t_n} & 0 \\ 0 & 0 & 0 & e^{i\frac{\omega}{c}N_{z4}^{(n)}t_n} \end{bmatrix} . \tag{1.58}$$

The equation (1.56) can further be rewritten as

$$\boldsymbol{E}_0^{(n-1)}(z_{n-1}) = (\boldsymbol{D}^{(n-1)})^{-1}\boldsymbol{D}^{(n)}\boldsymbol{P}^{(n)}\boldsymbol{E}_0^{(n)}(z_n) = \boldsymbol{T}^{(n-1,n)}\boldsymbol{E}_0^{(n)}(z_n)\,, \tag{1.59}$$

through which the transfer matrix $\boldsymbol{T}^{(n-1,n)}$ has been defined. The transfer matrix binds together the field components in the adjacent layers. The transfer matrix can be constructed for all interfaces with the exception of the last interface with the substrate half-space. The substrate is considered semi-infinite and thus, the propagation matrix can not be constructed. The transfer matrix for the last interface is defined as

$$\boldsymbol{E}_0^{(N)}(z_N) = (\boldsymbol{D}^{(N)})^{-1}\boldsymbol{D}^{(N+1)}\boldsymbol{E}_0^{(N+1)}(z_N) = \boldsymbol{T}^{(N,N+1)}\boldsymbol{E}_0^{(N+1)}(z_N)\,. \tag{1.60}$$

The anisotropic multilayer can now be characterised by a single matrix $\boldsymbol{M}$ obtained implicitly from (1.59) and (1.60) as

$$\boldsymbol{E}_0^{(0)}(z_0) = \left(\prod_{n=1}^{N+1}\boldsymbol{T}^{(n-1,n)}\right)\boldsymbol{E}_0^{(N+1)}(z_N) = \boldsymbol{M}\boldsymbol{E}_0^{(N+1)}(z_N)\,. \tag{1.61}$$

For the final touch let us assume that the incident light wave can be decomposed into two orthogonal polarizations (eigenvectors) $\boldsymbol{e}_1^{(0)}$ and $\boldsymbol{e}_3^{(0)}$ with amplitudes $E_{01}^{(0)}$ and $E_{03}^{(0)}$ corresponding to the previously defined s and p-polarizations. Analogously let us assume two orthogonal polarizations $\boldsymbol{e}_2^{(0)}$ and $\boldsymbol{e}_4^{(0)}$ describing the reflected wave. Further assuming this superposition to hold true for the substrate half-space the amplitudes $E_{02}^{(N+1)}$ and $E_{04}^{(N+1)}$ must be zero since there is no light source or reflection. The equation (1.61) element-wise is then

$$\begin{bmatrix} E_{01}^{(0)} \\ E_{02}^{(0)} \\ E_{03}^{(0)} \\ E_{04}^{(0)} \end{bmatrix} = \begin{bmatrix} M_{11} & M_{12} & M_{13} & M_{14} \\ M_{21} & M_{22} & M_{23} & M_{24} \\ M_{31} & M_{32} & M_{33} & M_{34} \\ M_{41} & M_{42} & M_{43} & M_{44} \end{bmatrix} \begin{bmatrix} E_{01}^{(N+1)} \\ 0 \\ E_{03}^{(N+1)} \\ 0 \end{bmatrix} . \tag{1.62}$$

The reflection coefficients of the sample can be calculated from (1.62) and their respective definitions (1.20)-(1.23) as

$$r_{ss} = \left(\frac{E_{02}^{(0)}}{E_{01}^{(0)}}\right)_{E_{03}^{(0)}=0} = \frac{M_{21}M_{33} - M_{23}M_{31}}{M_{11}M_{33} - M_{13}M_{31}}, \tag{1.63}$$

$$r_{sp} = \left(\frac{E_{02}^{(0)}}{E_{03}^{(0)}}\right)_{E_{01}^{(0)}=0} = \frac{M_{11}M_{23} - M_{21}M_{13}}{M_{11}M_{33} - M_{13}M_{31}}, \tag{1.64}$$

$$r_{ps} = -\left(\frac{E_{04}^{(0)}}{E_{01}^{(0)}}\right)_{E_{03}^{(0)}=0} = -\frac{M_{41}M_{33} - M_{43}M_{31}}{M_{11}M_{33} - M_{13}M_{31}}, \tag{1.65}$$

$$r_{pp} = -\left(\frac{E_{04}^{(0)}}{E_{03}^{(0)}}\right)_{E_{01}^{(0)}=0} = -\frac{M_{11}M_{43} - M_{41}M_{13}}{M_{11}M_{33} - M_{13}M_{31}}. \tag{1.66}$$

Using the reflection coefficients, we can calculate the magneto-optical response of the sample from (1.24) and (1.29) for our arbitrary multilayer sample.

For the purpose of this thesis, it is more important to model the off-diagonal element of the permittivity tensor from the diagonal element and the magneto-optical response. This can not be achieved analytically. The least square method can be utilized with the presented approach to model the off-diagonal element of the permittivity tensor.

2. Introduction to magnetism

This chapter provides a basic introduction to magnetism with a focus on ferromagnetism and the origins of ferromagnetism in LSMO. Magnetic properties of materials result from an alignment of atomic magnetic moments. A sketch of different types of alignment can be seen in Fig. 2.1. In the case of paramagnetism, the magnetic moments are aligned randomly, and no net magnetic moment is present. Ferromagnetic materials align parallel creating a net magnetic moment. Ferrimagnetic materials also have a net magnetic moment; however it is a result of two or more uneven magnetic sublattices that prefer anti-parallel orientation. Lastly, the infamously useless[1] anti-ferromagnetic ordering consists of multiple sublattices that compensate for one another resulting in zero magnetic moment.

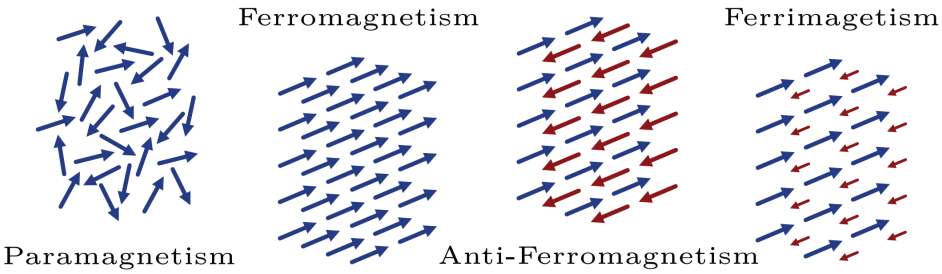

Figure 2.1: Illustration of different types of magnetic ordering taken from. Colour illustrates different magnetic sublattices. Figure taken from [9].

2.1 Ferromagnetism

Atomic magnetic moments in ferromagnetic materials align parallel to each other. The moments are generally not aligned throughout the whole material; instead, they form areas with parallel alignment called domains. If a ferromagnetic material has not previously been exposed to a magnetic field the magnetic domains are randomly oriented, and their magnetic moments cancel out. This is a so-called virgin state. When an external field is applied, the magnetization of the material follows a non-linear hysteresis loop (see Fig. 2.2) that is dependent on the history of the material. Multiple values are used to characterise this curve. Saturation magnetization M_s is the magnetization value when all domains are oriented in the same direction. Remanent magnetization M_r is magnetization in the absence of an external magnetic field, and coercivity field H_c is the external field necessary for zero magnetization of the material.

The shape of the hysteresis loop of a ferromagnet is dependent on the direction of magnetization. This is called magnetic anisotropy. Magnetic anisotropy describes different magnetic properties of materials depending on their orientation. Ferromagnetic materials can exhibit one easy axis along which they are easiest to magnetize. In this direction, the coercivity field and remanence are highest.

[1] In his Nobel prize speech in 1970 awarded for the work and discoveries in antiferromagnetism Louis Néel described them as interesting but useless.

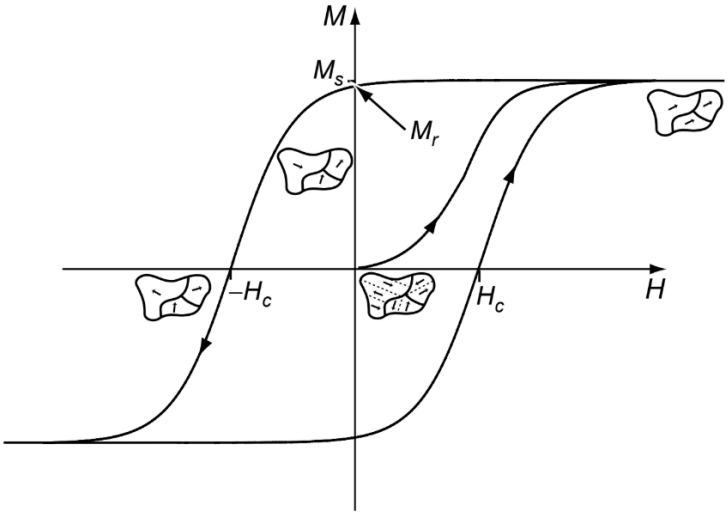

Figure 2.2: Hysteresis loop of a ferromagnetic material. Initially in a demagnetized virgin state. With the introduction of external magnetic field H the magnetic moments of domains begin to align until they reach saturation magnetization M_s. Remanent magnetization M_r is magnetization in the absence of external magnetic field. Coercivity field H_c is the external field necessary to reduce the magnetization to zero. Figure taken from [13].

2.2 Curie temperature

With increasing temperature remanent magnetization of ferromagnetic materials decreases. At a certain temperature the magnetization drops sharply to zero. We call this temperature the Curie temperature T_C. At this temperature a second-order phase transition takes place. It is a transition between the ferromagnetic and paramagnetic states. At the Curie temperature the atomic magnetic moments stop forming domains and become randomly oriented as thermal disorder overcomes the exchange interaction.

2.3 Double-exchange interaction

The ferromagnetism of LSMO has been explained by C. Zener [4] through double-exchange interaction (DE). This mechanism originates from an e_g electron transfer between Mn^{3+} and Mn^{4+} ions via a O^{2-} $2p$ state. The probability of the electron transfer is higher between manganese atoms with the same spin orientation of unpaired electrons (i.e., the e_g electron does not need to reorient its spin during the transfer). If the probability of the transfer is higher, then the electron is less localised and hence has lower energy. As a result of the material minimizing its energy, the spins of the manganese unpaired electrons align and form domains.

3. Experimental techniques

This chapter provides an overview of the utilized experimental methods. The following methods were used to prepare the thin film samples, examine the quality of their deposition and evaluate their magnetic, optical, and magneto-optical properties.

3.1 Pulsed laser deposition

Pulsed laser deposition (PLD) is a widely used method for the deposition of high-quality thin films. A schematic sketch of the method can be seen in Fig. 3.1. The desired material is placed inside a vacuum chamber in the form of a dense target. The target is then impacted and ablated by a high-energy laser pulse. The ablated material creates a plasma plume propagating upward. Upon reaching the heated substrate, the plume condensates.

In order to achieve epitaxial growth, the ablated plume must consist mostly of atomic, diatomic, and other low-mass components. This is aided by the use of a nanosecond laser pulse in the ultraviolet range, which is strongly absorbed by a small portion of the ceramic target. Other targets (e.g., polymers, organic materials) require different conditions.

PLD method operates with a background gas. In the case of oxide films, an oxygen atmosphere is used. The oxygen serves two purposes. Firstly it helps provide proper stoichiometry of the fabricated films. Secondly, it lowers the energy of the particles in the plume in order not to damage the structure of the film upon impact [14]. Post-deposition oxygen annealing is also employed in order to oxidize the film or on the contrary to remove extra oxygen. This post-deposition treatment has been shown to improve the Curie temperature and colossal magnetoresistance of the film [15].

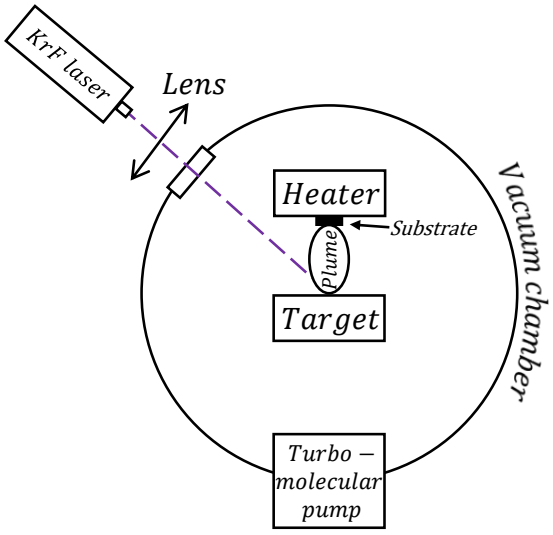

Figure 3.1: Schematic depiction of a pulsed laser deposition setup. A high energy pulsed KrF laser impacts a dense target creating a plasma plume. The plume condenses on a heated substrate creating a thin film.

3.2 Atomic force microscopy

Atomic force microscopy (AFM) is a type of scanning probe microscopy. Scanning with a physical probe allows it to go several orders of magnitude higher in precision compared to diffraction-limited optical microscopes [16].

The principle of operation is the van der Waals interaction between a sharp tip of the probe and the sample surface. The backside of the probe serves as a mirror that reflects an incident laser beam into a position-sensitive photodiode (see Fig. 3.2). This allows for high precision measurements of the cantilever position. The surface scanning is accomplished by moving the piezoelectric stage with the sample.

The atomic force microscope can work in three different modes. The simplest is the contact mode. In this mode the cantilever is static and it is dragged along the surface of the material whilst in direct contact with it. This causes the cantilever to bend corresponding to the surface height and change the reflection of the incoming laser beam. The relative surface height can be deduced from the change of intensity on the position-sensitive photodiode. Alternatively, the intensity on the photodiode can be kept constant by moving the cantilever up and down using a piezoelectric device. In that case, the height can be deduced from the adjustment.

The second option is the tapping mode in which the cantilever is set to oscillate (using piezoelectric components, magnetic field, or by periodic heating) at its resonant frequency with a constant amplitude. Upon contact with the surface, the amplitude of the oscillations changes (generally it decreases). By moving the cantilever up and down using the piezoelectric device, the amplitude can be maintained at a constant value, and the surface topography can be reproduced. The tapping mode, while exerting higher pressure during contact, is generally less damaging as the lateral forces acting upon the sample are much smaller.

Lastly, the non-contact mode utilizes a similar principle as the tapping mode; however, in this mode the tip does not come into contact with the surface. Much like in the tapping mode, we maintain the frequency and the amplitude constant and determine the surface topography from the vertical adjustments to the cantilever position. In this mode adsorbed fluid on the sample surface can cause severe changes to the measured topography; hence this mode is generally reserved for delicate samples.

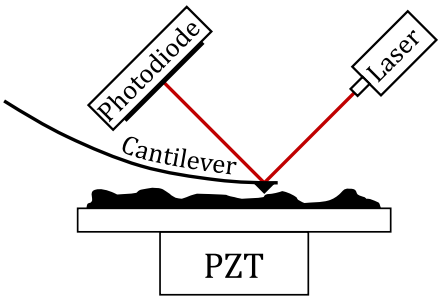

Figure 3.2: Sketch of the atomic force microscopy setup. Atomic forces act upon the tip of the cantilever and bend it. The change in the cantilever position is detected using a laser beam reflected on the backside of the cantilever.

3.3 X-ray diffraction

X-ray diffraction (XRD) is a characterization technique evaluating the crystallographic structure and crystalline quality of investigated materials. The method is based on detecting X-rays diffracted on lattice planes of the sample. The peak intensity of diffracted radiation follows the Bragg law

$$2d_{hkl} \sin\theta = \lambda\,, \tag{3.1}$$

where d_{hkl} is the difference between two lattice planes given by Miller indices hkl, angle θ is the angle of incidence for which peak intensity occurs and λ is the wavelength of X-ray radiation.

A sketch of the XRD setup can be seen in Fig. 3.3. Several angles of rotation are depicted. Rotating the sample in the plane of incidence is denoted by angle ω. The rotations outside the plane of incidence are denoted by angles φ and ψ. Angle 2θ is taken as the angle between the incident and reflected X-ray.

The most basic of XRD measurements is a symmetric θ-2θ scan. During this scan the X-ray source is kept at a set position. The detector and sample are adjusted so that $\psi = 0$ and $\omega = \theta$. In this geometry detected X-rays are being diffracted on the lattice planes parallel to the sample surface. This provides information about the out-of-plane lattice parameter of the sample [17].

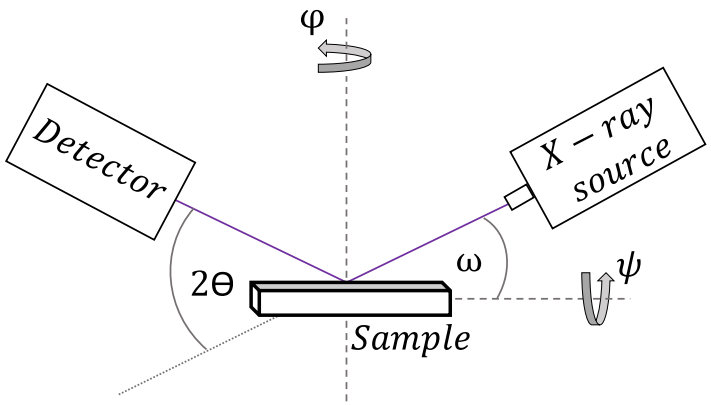

Figure 3.3: Sketch of an X-ray diffraction setup. Angles ω, φ and ψ define rotation of the sample. Angle 2θ defines the detection angle.

3.4 Vibrating-sample magnetometer

Vibrating-sample magnetometer (VSM) is a precise yet quite simple measurement setup for detecting small magnetic signal. VSM utilizes the Faraday law of induction to measure the magnetization of a sample. The sample is placed on a rod in a uniform magnetic field sustained by a superconducting electromagnetic coil (see Fig. 3.4). The magnetic dipole moment of the sample aligns with the external magnetic field, creating a magnetic field of the sample. If the rod with the sample is vibrating, the magnetic field of the sample changes in time. The

change of the magnetic field induces alternating current (AC) in the pick-up coils. In order to separate signal from noise, the current passes through a lock-in amplifier that is tuned to the sample vibration frequency. Signal coming from the lock-in amplifier can then be tied back to the magnetic moment of the sample and can be separated from the noise for values as low as 10^{-6} emu.

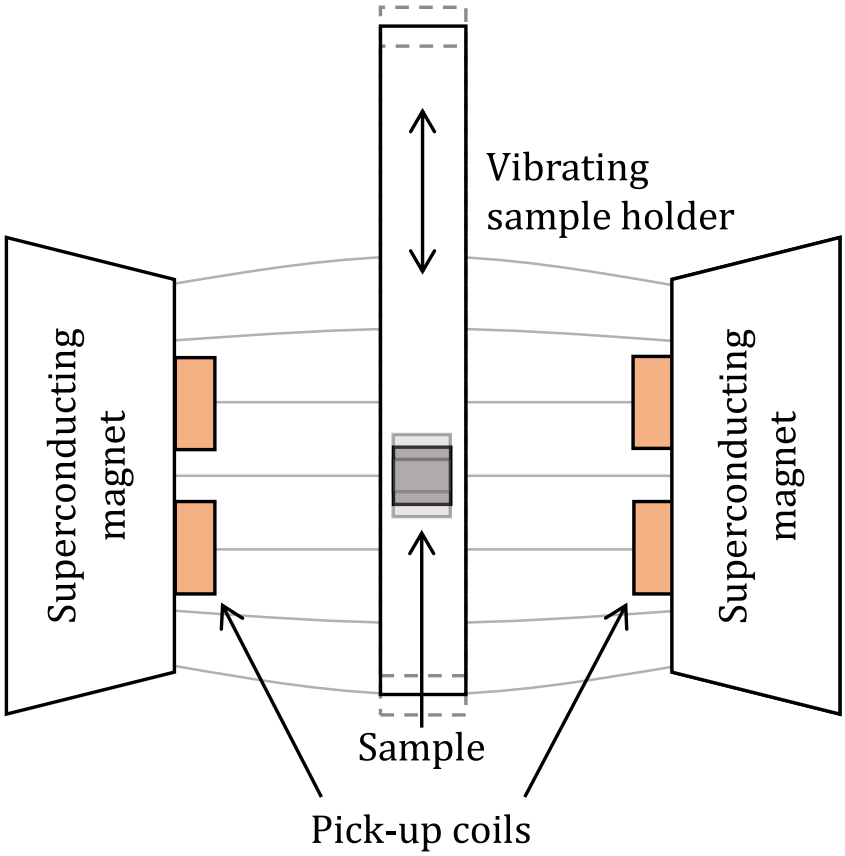

Figure 3.4: Schematic depiction of a vibrating-sample magnetometry measurement technique.

3.5 Spectroscopic ellipsometry

Spectroscopic ellipsometry is a measurement technique analyzing the optical response of a sample. It is capable of measuring a full Mueller matrix of a sample or numerically model the isotropic scalar permittivity of a single layer in a multilayer sample.

The measurement method uses a wide spectrum lamp concentrated upon the surface of the sample (see Fig. 3.5). Before the beam impacts the sample, it passes through a polarizer P and optionally a compensator C_{opt} (waveplate). After reflection off the sample surface S, the beam propagates through a compensator C (waveplate), an analyser A (polarizer), and finally reaches a spectrally sensitive detector D.

Let us consider the Jones matrices of the optical components. We will work in the Cartesian coordinate system defined in Fig. 1.2. We shall omit the optional

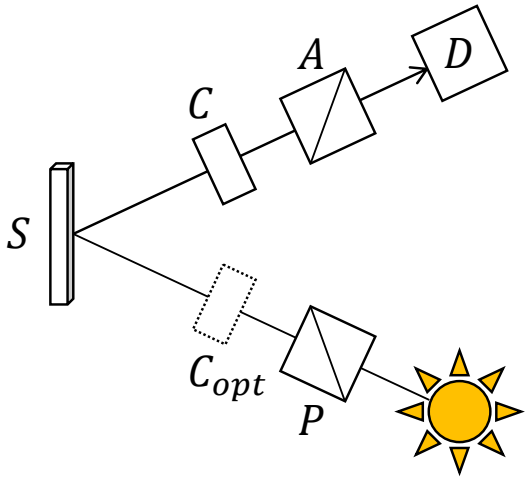

Figure 3.5: Sketch of a spectroscopic ellipsometry setup. Light from a wide-spectrum lamp passes through a polarizer P, reflects off a sample S and continues through a compensator C, analyzer A and into the detector D. Optionally an aditional compensator C_{opt} can be added before sample reflection.

compensator. Let the polarizer P be oriented at an angle ξ with respect to the $\boldsymbol{x}$ axis. Its Jones transmission matrix is

$$\boldsymbol{T}_P = \begin{bmatrix} \cos^2\xi & \sin\xi\cos\xi \\ \sin\xi\cos\xi & \sin^2\xi \end{bmatrix} . \tag{3.2}$$

If we consider an optically isotropic sample, then the reflection matrix of the sample is given by

$$\boldsymbol{R}_s = \begin{bmatrix} r_{ss} & 0 \\ 0 & r_{pp} \end{bmatrix} . \tag{3.3}$$

Let the waveplate have a retardance Γ. The retardance is spectrally dependent. If the principal axes are aligned with s and p-polarizations, then its transmission matrix takes the form

$$\boldsymbol{T}_C = \begin{bmatrix} e^{i\Gamma} & 0 \\ 0 & 1 \end{bmatrix} . \tag{3.4}$$

Lastly, let the analyser be oriented at an angle ζ with respect to the $\boldsymbol{x}$ axis. Similarly to (3.2) the transmission matrix is

$$\boldsymbol{T}_A = \begin{bmatrix} \cos^2\zeta & \sin\zeta\cos\zeta \\ \sin\zeta\cos\zeta & \sin^2\zeta \end{bmatrix} . \tag{3.5}$$

The relation between the initial Jones vector $\boldsymbol{J}^{(I)}$ and the final Jones vector $\boldsymbol{J}^{(F)}$ is given by the product of matrices of the optical elements as

$$\boldsymbol{J}^{(F)} = \boldsymbol{T}_A \cdot \boldsymbol{T}_C \cdot \boldsymbol{R}_s \cdot \boldsymbol{T}_p \cdot \boldsymbol{J}^{(I)} \,. \tag{3.6}$$

Detected intensity of light is then given by

$$\boldsymbol{I} = (\boldsymbol{J}^{(F)})^* \boldsymbol{J}^{(F)} \,. \tag{3.7}$$

Spectroscopic ellipsometry investigates the change in polarization upon reflection off the sample. That change is represented by the ratio of diagonal elements of the reflection matrix of the sample. This ratio is defined as

$$\rho \equiv \frac{r_{pp}}{r_{ss}} = \tan \Psi e^{i\Delta} \,, \tag{3.8}$$

where we also introduced ellipsometric angles Ψ and Δ. Ellipsometric angles can be extracted from the intensity of the detected light. That is achieved through rotating one or more components of the setup. Intensity is a function of the angle of rotation of the optical element. Ellipsometric angles are parameters of this function. The full calculation can be seen elsewhere [18].

From ellipsometric angles, the diagonal element of the permittivity tensor can be modelled using software. In addition to optical properties, the thickness of a sample layer can be estimated. Generally, we characterise one layer of a sample with full knowledge of the optical and physical properties of the other layers.

3.6 Magneto-optical spectroscopy

Magneto-optical spectroscopy is a highly sensitive method for measuring the magneto-optical Kerr effect. The ability to measure magneto-optical angles with millidegree precision makes it suitable for the measurement of ultrathin films. Magneto-optical spectroscopy is also a surface technique mitigating the magnetic influence of the substrate.

The measurement setup (see Fig. 3.6) is very similar to that of spectroscopic ellipsometry. Analogously to ellipsometry, we investigate the change in polarization upon reflection off the sample. However, in spectroscopic ellipsometry we assumed the sample to be isotropic and the polariser to allow both s and p polarizations to pass. In magneto-optical spectroscopy we use an external magnetic field to magnetize the sample and induce optical anisotropy. Thus the incident light on the sample is strictly s or strictly p-polarised in order to measure the off-diagonal reflection coefficient.

For the purpose of this thesis, we shell consider polar geometry with almost normal incidence. The angle of incidence of the setup is low enough to justify (1.34) yet allows for spatial differentiation between the incident and reflected light beams. In terms of Jones calculus the reflection matrix of the magnetized sample takes the form

$$\boldsymbol{R} = \begin{bmatrix} 1 & -\Phi_k \\ -\Phi_k & -1 \end{bmatrix} \,. \tag{3.9}$$

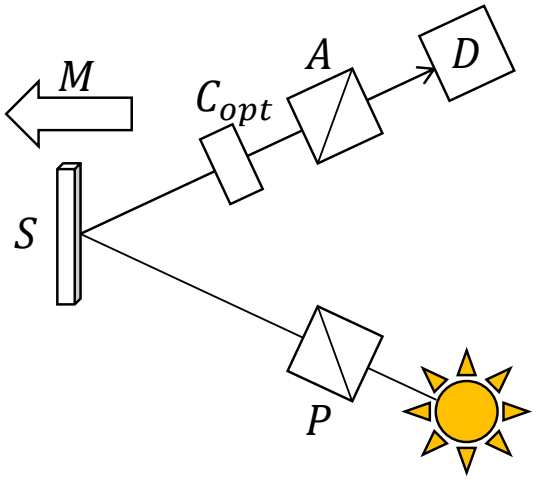

Figure 3.6: Sketch of a magneto-optical spectroscopy setup in polar configuration. Light from a wide-spectrum lamp passes through a polarizer P, reflects off a magnetized sample S and continues through an optional compensator C_{opt}, analyzer A and into a spectrally sensitive detector D.

Let the polarizer P, with Jones transmission matrix (3.2), be rotated 90° allowing only *p*-polarized light. If we neglect the overall amplitude, we can use (3.4) and (3.5) to write the relation between the initial and the final Jones vectors as

$$\boldsymbol{J}^{(F)} = \begin{bmatrix} \cos^2\zeta & \sin\zeta\cos\zeta \\ \sin\zeta\cos\zeta & \sin^2\zeta \end{bmatrix} \begin{bmatrix} e^{i\Gamma} & 0 \\ 0 & 1 \end{bmatrix} \begin{bmatrix} 1 & -\Phi_k \\ -\Phi_k & -1 \end{bmatrix} \begin{bmatrix} 0 & 0 \\ 0 & 1 \end{bmatrix} \boldsymbol{J}^{(I)}\,, \tag{3.10}$$

$$\boldsymbol{J}^{(F)} = \begin{bmatrix} -e^{i\Gamma}\Phi_k\cos^2\zeta - \sin\zeta\cos\zeta \\ -e^{i\Gamma}\Phi_k\sin\zeta\cos\zeta - \sin^2\zeta \end{bmatrix}. \tag{3.11}$$

Intensity of the detected signal can be calculated using (3.7) as

$$I = \sin^2\zeta + |\Phi_k|^2\cos^2\zeta + \sin(2\zeta)\,\mathrm{Re}\left\{\Phi_k e^{i\Gamma}\right\}. \tag{3.12}$$

The second-order term $|\Phi_k|^2$ can be neglected as the MOKE generally has a small magnitude. Using this approximation, the intensity in terms of the magneto-optical angles can be written as

$$I = \sin^2\zeta + (\theta_k\cos\Gamma + \epsilon_k\sin\Gamma)\sin(2\zeta)\,. \tag{3.13}$$

Using the above relation, it is possible to measure the magneto-optical Kerr effect by measuring intensity as a function of the rotation of the analyzer. One must also not forget that we omitted the absolute magnitude of light intensity.

Accuracy can be further improved by measuring in both polarities of magnetization. By taking the difference of the measured Kerr angles, the unwanted influence of optical effects and quadratic magneto-optical effects can be eliminated.

4. Investigated samples

The magnetic oxide samples investigated in this thesis are $La_{2/3}Sr_{1/3}MnO_3$ (LSMO) thin films on various substrates. In this chapter, we introduce the bulk properties of LSMO and comment on the subject of strain impact on thin films.

4.1 Bulk LSMO

The ideal crystallographic structure of manganese oxides is cubic perovskite (see Fig. 4.1). The perovskite structure belongs to $Pm\bar{3}m$ space group (No. 221). The stability of a manganese oxide structure follows the tolerance factor

$$t = \frac{r_A + r_O}{\sqrt{2(r_B + r_O)}}, \tag{4.1}$$

where r_A, r_B, and r_O are the ionic radii of the A,B, and oxygen atoms, respectively. For an ideal cubic perovskite, the tolerance factor is equal to unity. However, due to the variation in cation ionic radii the tolerance factor usually diverges from this value significantly. That leads to an orthorhombic or rhombohedral structure. If the tolerance factor differs crucially, then the structure becomes unstable. The structure has been shown to be stable for $0.89 < t < 1.02$ [19].

Unit cell of bulk LSMO is in fact rhombohedral with lattice constants $a_r = 5.471$ Å and $\alpha_r = 60.43°$ [20]. This structure belongs in the $R\bar{3}c$ space group (No. 167).

The level of strontium doping of $LaMnO_3$ has been chosen based on the work of Jonker and van Santen [3] who demonstrated that doping with $\frac{1}{3}$ of Sr provides the highest Curie temperature of 370 K.

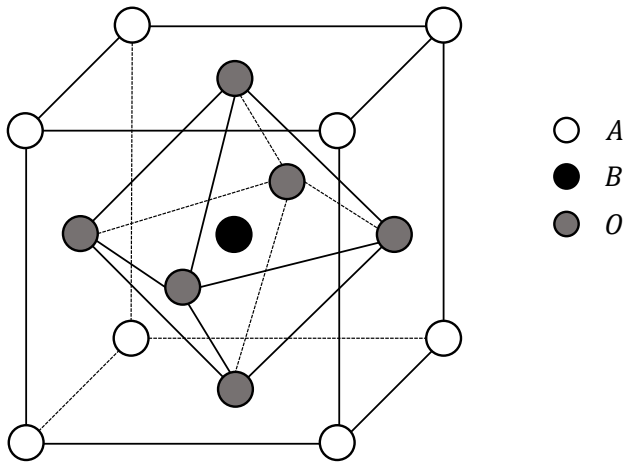

Figure 4.1: Schematic sketch of an ideal cubic perovskite structure of ABO_3.

4.2 Substrate materials

Depositing materials as thin films impacts their physical properties. In the case of epitaxial growth, the material accommodates its in-plane lattice parameters to correspond to the lattice parameters of the substrate. As such, substrates with close lattice parameters need to be chosen. For the purpose of this thesis, cubic (001) oriented $SrTiO_3$ (STO) and a tetragonal (001) oriented $BaTiO_3$ (BTO) substrates have been used for epitaxial growth. Their lattice parameters are higher than that of the pseudocubic parameters of LSMO (see Table 4.1), and thus they exert tensile strain. The level of tensile strain can be evaluated through a lattice mismatch parameter

$$m = \frac{a_l - a_s}{a_s}\,, \tag{4.2}$$

where a_l and a_s are the lattice parameters of the thin layer and the substrate, respectively. The sign of the lattice mismatch parameter carries information on the type of strain. A positive sign refers to compressive strain, while a negative sign means tensile strain.

Material	LSMO	STO	BTO
Lattice parameter a [Å]	3.876	3.905	3.995
Lattice mismatch m [%]	-	-0.74	-2.98

Table 4.1: Comparison of pseudocubic lattice parameters of LSMO [21] and the substrates STO and BTO [22].

Textured samples of LSMO have been deposited by PLD on a silicon substrate with the aid of a seed nanosheet (NS) layer. A seed layer is used because of the high lattice mismatch between silicon and LSMO. The nanosheet layer is made of a singular layer of $Ca_2Nb_3O_{10}$. The introduction of a seed NS layer allows for close to epitaxial growth of LSMO on any substrate regardless of its crystalline quality (thin films on LSMO have already been grown on an amorphous substrate using this approach [23]). We demonstrate this through the growth of LSMO thin films on a silicon substrate.

4.3 Influence of epitaxial strain

The epitaxial strain has been shown to influence the orbital ordering of the manganese $3d$ levels in LSMO [24]. A schematic sketch of the Mn energy levels for different symmetries can be seen in Fig. 4.2. An isolated manganese atom has all $3d$ energy levels degenerated. A partial lifting of degeneracy is achieved by placing the Mn atom inside the oxygen octahedra. For thin films subjected to tensile strain (e.g., grown on STO or BTO) further lifting of degeneracy occurs as the symmetry of the system is lowered. This affects only the Mn^{3+} ion as the Mn^{4+} prefers to keep t_{2g} energy levels unchanged in what is called the Jahn-Teller effect [19]. As the ferromagnetism in LSMO has been explained by the DE interaction, the change in the Mn $3d$ energy levels (as well as a possible change in

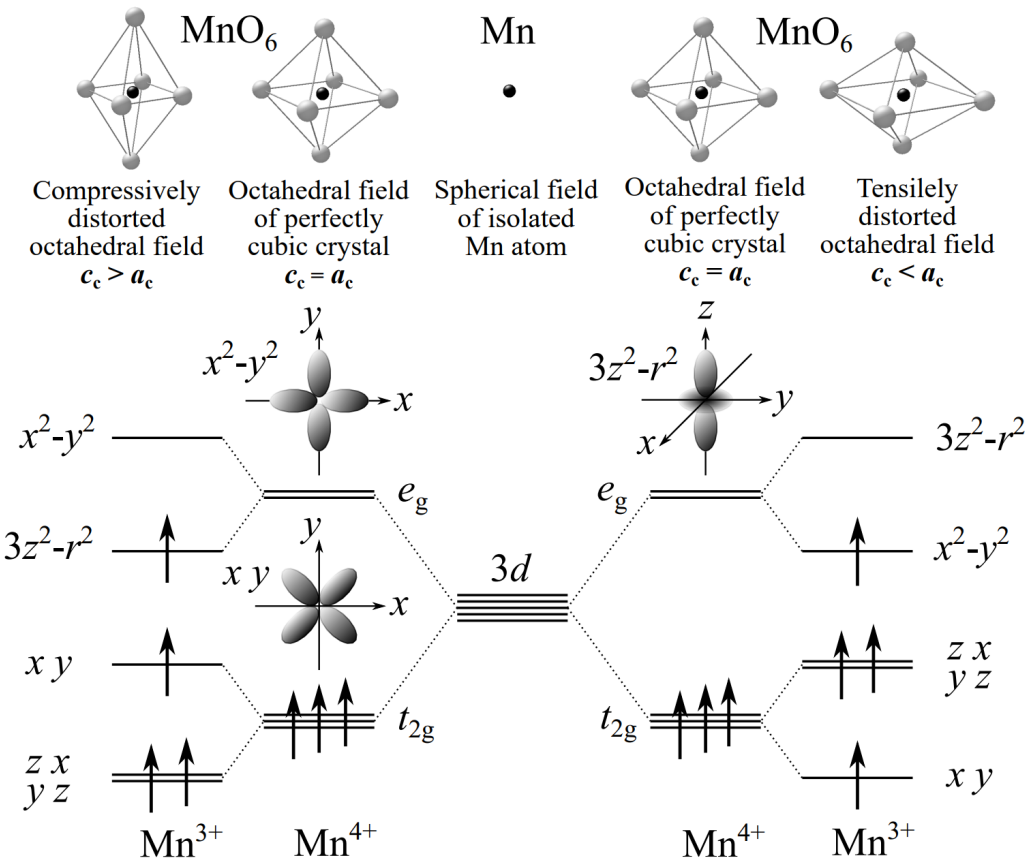

Figure 4.2: Illustration of the splitting of the manganese 3*d* energy levels. The degeneracy is partially lifted by the oxygen octahedra field. The Jahn-Teller effect further shows Mn^{3+} energy levels splitting for tensile and compressive distortion. Figure taken from [17].

the Mn^{3+} - O - Mn^{4+} geometry, orbital overlap, and bond length) influences the magnetic properties of LSMO.

Magnetic anisotropy of LSMO thin films also differs from that of bulk LSMO. Magnetization easy axis of bulk LSMO lies along the pseudocubic $[111]_c$ direction [25], whereas for thin films it typically rotates into the plane of the film. LSMO grown on STO indeed shows in-plane anisotropy with $\langle 100 \rangle_c$ and $\langle 110 \rangle_c$ being equivalent easy axis of magnetization above 250 K [26]. Bellow 250 K the $\langle 110 \rangle_c$ direction becomes magnetically easier.

Lastly, epitaxial strain and substrate symmetry induce oxygen octahedra rotations (OOR). OOR are rotations of the oxygen octahedra in the perovskite structure of LSMO. The influence of OOR on physical properties is still being debated as some works claim a positive correlation between the angle of octahedra tilt and magnetic properties of the film [27], where others claim the correlation to be negative [28].

5. Experimental results

This chapter will guide the reader chronologically from the process of fabrication, crystalline and surface quality examination, magnetic properties evaluation to optical and magneto-optical measurements, and the calculation and characterization of the permittivity tensor of LSMO thin films on various substrates. Additionally, temperature-dependent optical and magneto-optical properties of a selected sample will be presented and described.

5.1 Thin film fabrication

Samples of LSMO thin films on three different substrates have been prepared by PLD at the Centre for Nanoscience and Nanotechnology in Orsay. The depositions on STO, BTO, and buffered silicon substrates have been done under similar conditions with a varying number of pulses to achieve multiple thicknesses of LSMO layers. Six samples of LSMO on STO have been prepared, although in this thesis we focus on only three with the most relevant thicknesses. One sample of LSMO on BTO was prepared, along with two samples of LSMO on NS on Si.

The PLD setup used a KrF ultraviolet laser operating at $\lambda = 248$ nm. The pulse repetition rate was set to 2 Hz. The energy of the laser was 300 mJ with a 6×15 cm mask. The pressure of the oxygen atmosphere was 110 mTorr during the deposition and 75 Torr during the post-deposition annealing. The substrate temperature was maintained at 720 K.

Substrate heating is essential to achieve epitaxial growth; however, that means heating the BTO substrate well above the temperature of its structural transition [29]. This, unfortunately, resulted in the creation of ferroelectric $a - c$ domains with a misorientation angle that prevented perfect growth and optical measurements of LSMO on the BTO substrate.

5.2 Crystalline properties

All samples have been investigated using a PANanalytical X'Pert PRO diffractometer with a Cu anode and a wavelength of $\lambda = 1.5406$ Å. The geometry of the XRD measurement was set to the symmetric $\theta - 2\theta$ scan around the (002) Bragg reflection of LSMO. To evaluate film thickness t and out-of-plane pseudocubic parameter c_c an interference formula was used

$$I = I_0 \left[\frac{\sin \frac{2\pi}{\lambda} t \sin\theta}{\sin \frac{2\pi}{\lambda} c_c \sin\theta} \right]^2 . \tag{5.1}$$

This approach (called the kinematic approximation) supposes the superposition of intensities of the substrate and thin-film peak. However, in the case of LSMO on STO it has been shown [30] that the X-rays diffracted on the substrate interfere with the rays diffracted on the thin film. This results in a poor theoretical fit of our model, especially in the interference fringes on the side of the

substrate peak. Therefore a good fit of the interference fringes of higher angles is prioritized.

Three samples on the STO substrate have been deemed worthy of further research. They have been chosen based on their thicknesses measured by XRD. The $\theta - 2\theta$ scans of these three samples can be seen in Fig. 5.1 along with the theoretical fit. The resulting thicknesses and out-of-plane pseudocubic parameters can be seen in Table 5.1.

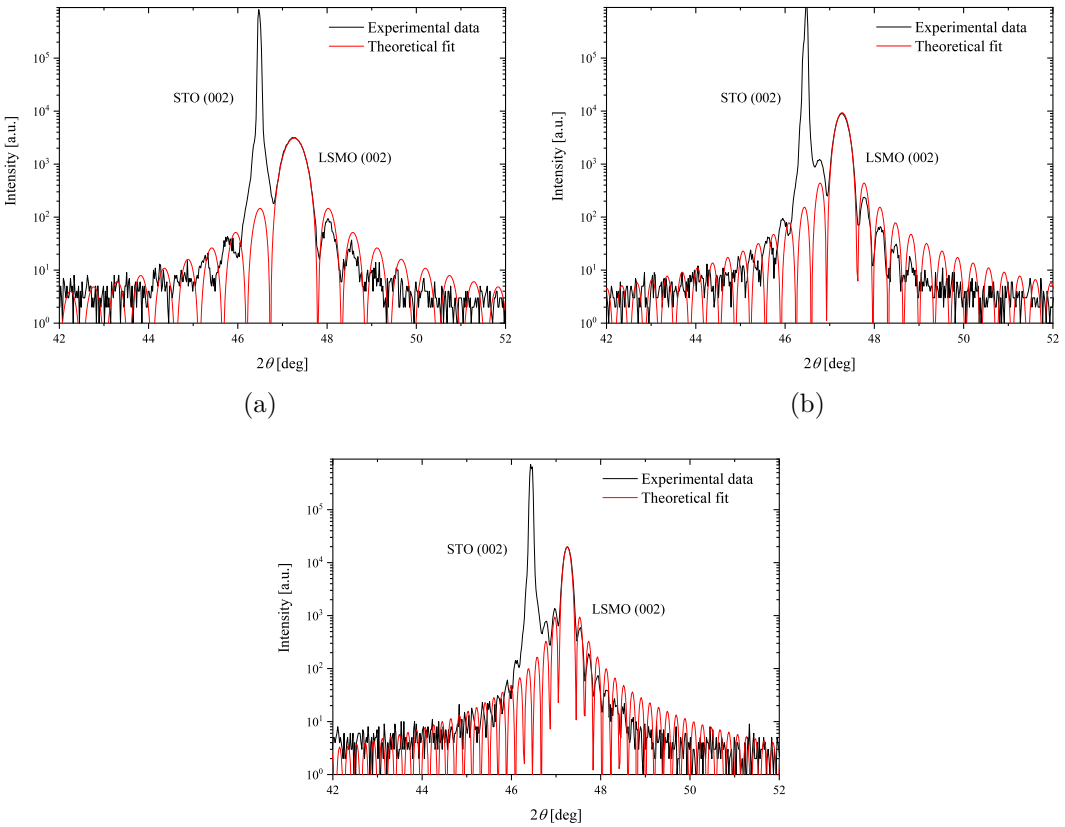

Figure 5.1: XRD $\theta - 2\theta$ measurements of LSMO on STO of thicknesses (a) 18.1 nm, (b) 28.0 nm and (c) 49.6 nm.

Sample	Thickness t [nm]	Out-of-plane latt. par. c_c [Å]
LSMO/STO	18.1	3.843
LSMO/STO	28.0	3.842
LSMO/STO	49.6	3.844
LSMO/NS/Si	$\sim$ 20	3.864
LSMO/NS/Si	$\sim$ 40	3.859

Table 5.1: Thicknesses and out-of-plane pseudocubic lattice parameters of LSMO layers as determined by XRD. Thicknesses of LSMO layers on Si could not be determined from XRD and are estimated from the number of pulses during deposition.

Thin films of LSMO grown on (100) oriented Si, with the aid of a NS seed layer, have been investigated by symmetric $\theta - 2\theta$ scans (see Fig. 5.2). They are expected to have a fiber structure with a unified out-of-plane component and random orientations in the in-plane direction (singular orientation on each nanosheet). A diffraction pattern consistent with the pseudocubic approximation has been observed. Out-of-plane lattice parameters have been determined from the position of the diffracted peaks (see Table 5.1). The pseudocubic parameters are significantly more relaxed than those of LSMO grown on STO. Thicknesses of the LSMO thin films on NS/Si could not be determined due to the lack of diffraction fringes caused by the textured nature of the films (carried over from the NS topology visible in Fig. 5.4). Approximate thicknesses of the samples can be estimated from the number of laser pulses used during deposition. The number of pulses would correspond to samples of 20 nm and 40 nm. Better estimates of sample thickness can be determined by spectroscopic ellipsometry in Section 5.5. Interestingly the lattice parameter of the thinner sample has been measured to be more relaxed than that of the thicker sample.

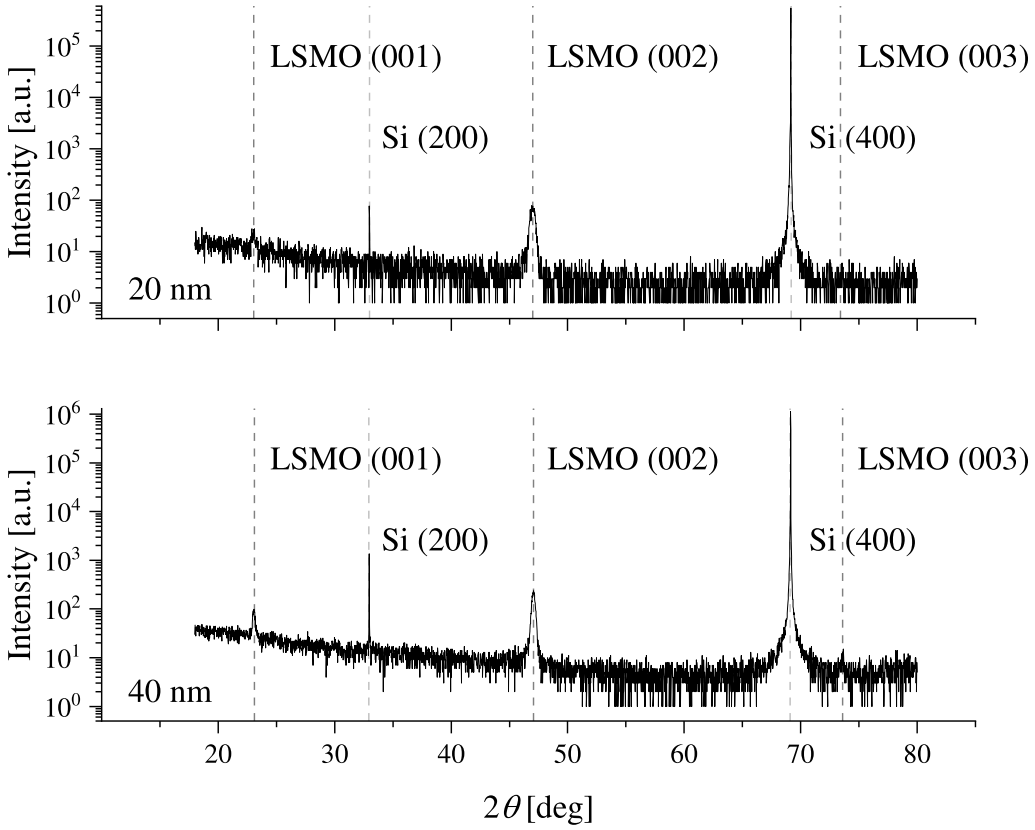

Figure 5.2: XRD $\theta - 2\theta$ measurements of LSMO on NS on Si of approximate thicknesses 20 nm (top) and 40 nm (bottom).

5.3 Surface quality

The surface of each sample and substrate has been examined by an Innova Bruker AFM in either contact or tapping mode.

The surface topology of the STO substrates, examined in contact mode, can be seen on the left side of Fig. 5.3. Surface roughness of the substrates is in order $R_{s18} = 0.17$ nm, $R_{s28} = 0.14$ nm and $R_{s50} = 0.20$ nm. Typical atomic steps can be seen on the last two substrates. Atomic steps are the result of miscut of the substrate, which is quite high for the substrate of the 28 nm thick layer 5.3(c). This does not impact the properties of LSMO thin films. The first substrate 5.3(a) shows very wide atomic steps with vacancy islands. Those are the result of inadequate annealing time after etching of the substrate. The islands did not have time to diffuse to the step edge due to its width. The size of the vacancy islands is larger than the LSMO nucleation length and does not impact epitaxial growth.

AFM measurements of the LSMO thin films deposited on STO can be seen on the right side of Fig. 5.3. All three samples copy the surface morphology of the substrates. Atomic steps are clearly visible on all samples, with vacancy islands visible on the 18 nm sample 5.3(b). Surface roughness of the LSMO layers is $R_{18} = 0.17$ nm, $R_{28} = 0.12$ nm and $R_{50} = 0.54$ nm. The thickest sample 5.3(f) exhibits droplets of LSMO of radius about 15 nm and height below 2 nm.

AFM of the NS/Si substrate, examined in tapping mode, can be seen in Fig. 5.4(a). The NS coverage is about 90 % with surface roughness $R_{NS} = 1.1$ nm being quite high given by the gaps between the NS. The substrate was made from a 1 cm $\times$ 1 cm Si wafer with chemically applied NS. It was cut into 5 mm $\times$ 5 mm pieces for LSMO deposition.

Thin films of LSMO deposited on NS/Si (see Fig. 5.4) follow the NS surface morphology with discernible textured growth. The surface roughness of the samples is $R_{NS\,20} = 0.48$ nm and $R_{NS\,40} = 0.74$ nm. The thicker sample 5.4(c) is displaying droplets on the surface with varying radii and height, with the largest droplets growing between the NS.

An image of the surface of LSMO deposited on top of BTO has been captured using a polarizing microscope (see Fig. 5.5). Nomarski contrast technique has been used to better show the structural modification of the surface caused by the ferroelastic domains.

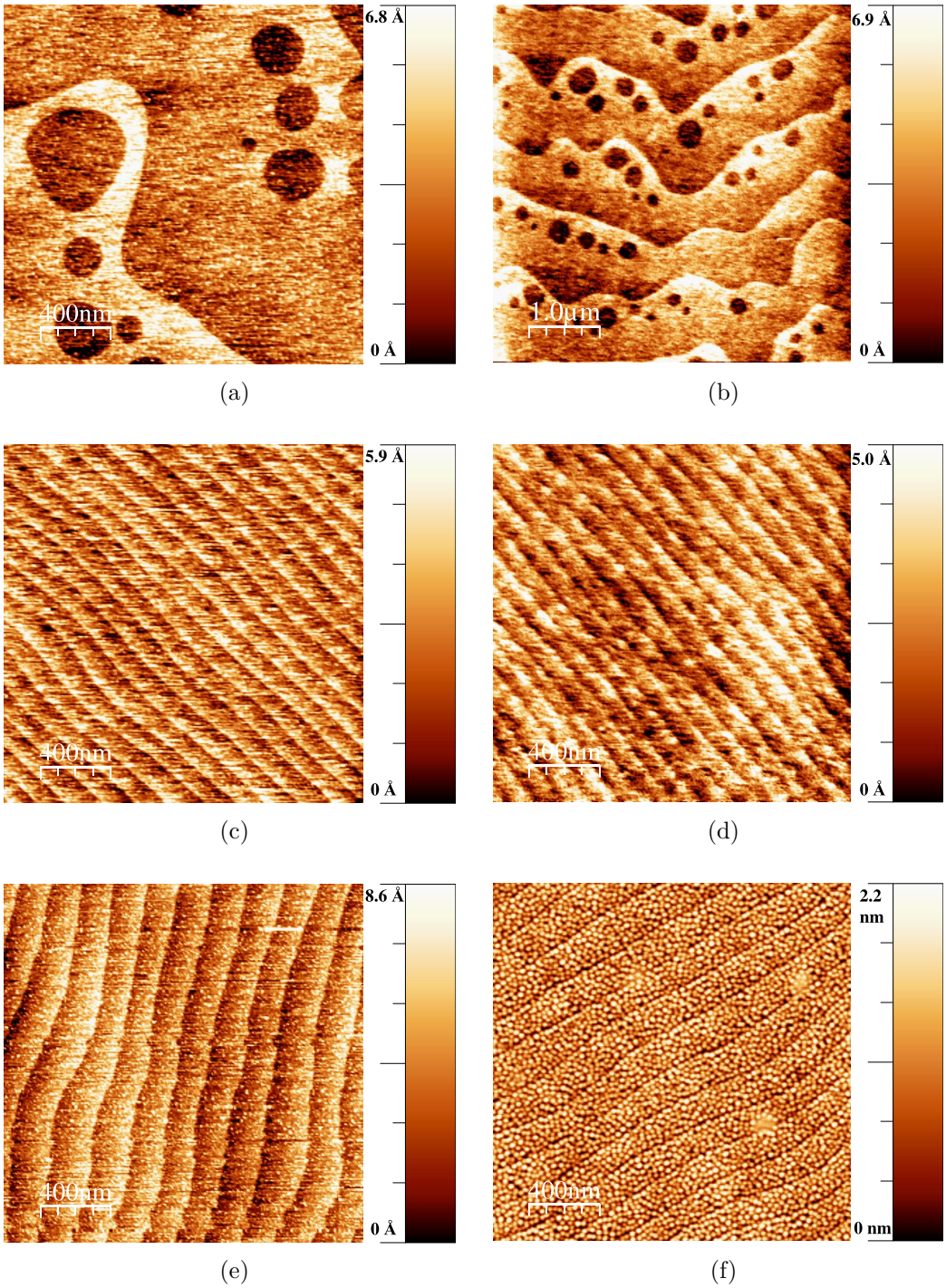

Figure 5.3: AFM images of STO substrates (a), (c) and (e) with corresponding thin films of LSMO (b), (d) and (f) of thicknesses 18.1 nm, 28.0 nm and 49.6 nm, respectively.

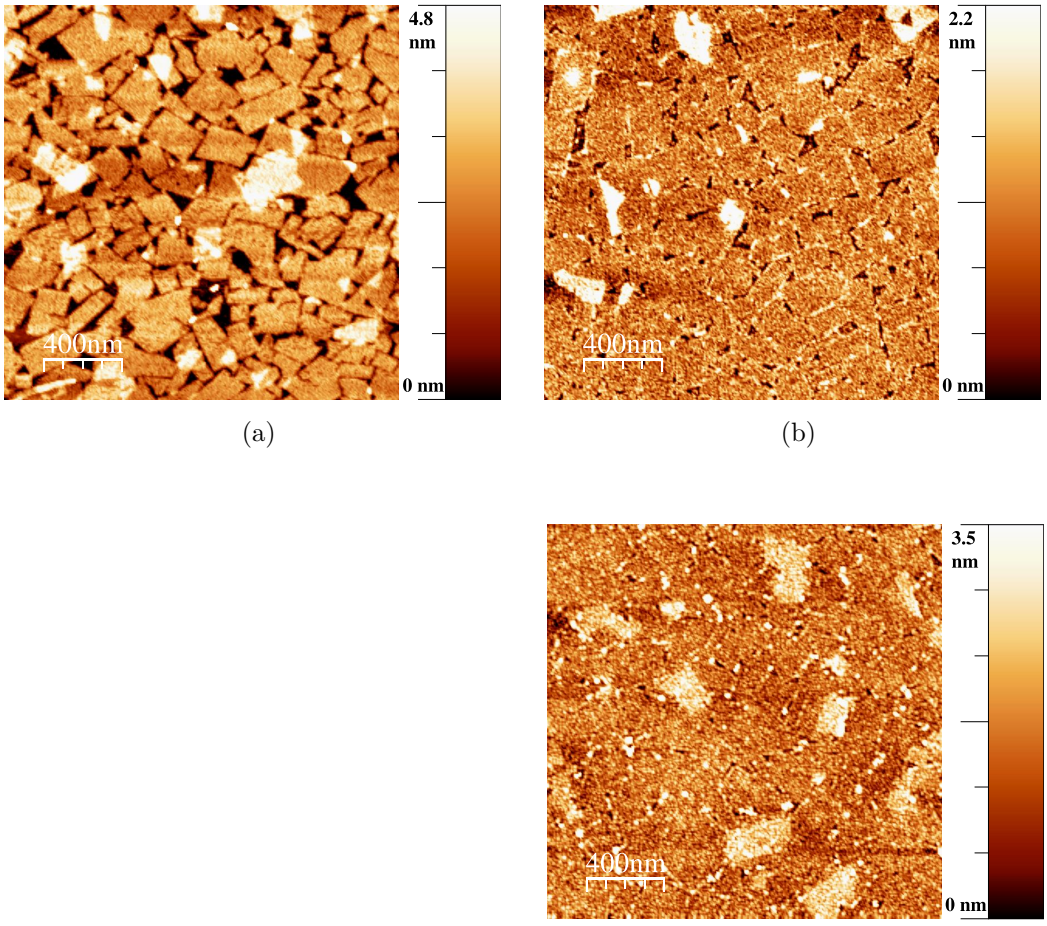

Figure 5.4: AFM images of the NS/Si substrate (a) and the thin films of LSMO (b) and (c) of approximate thicknesses 20 nm and 40 nm, respectively.

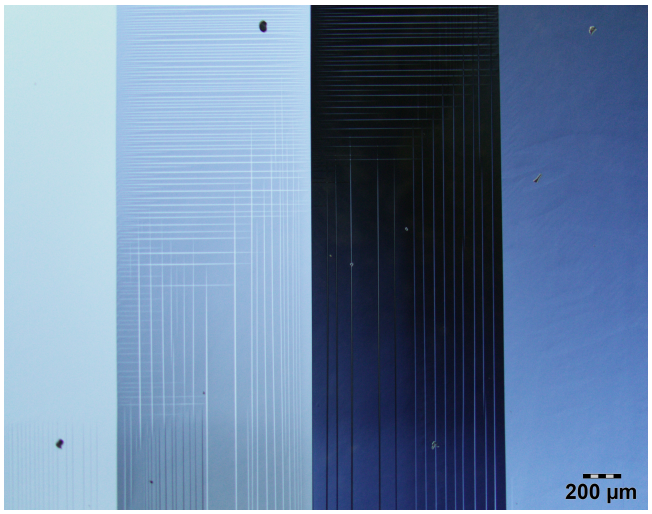

Figure 5.5: Nomarsky contrast microscopy image of the surface of LSMO grown on BTO. Structural modifications to the surface can be seen as a result of ferroelectric domain formation.

5.4 Magnetic properties

Magnetic properties of the investigated samples have been examined by a Physical Property Measurement System by Quantum Design equipped with a VSM option and a 9 T superconducting coil.

Magnetization measurements from 400 K to 3 K have been carried out with an in-plane external field of 0.2 T (see Fig. 5.6). The volume of the LSMO/NS/Si samples has been calculated using the thickness estimates from spectroscopic ellipsometry (see Section 5.5). The Curie temperature has been determined by a linear fit.

Magnetization of samples deposited on STO has a greater magnitude overall and differs only slightly between the samples. Samples on NS/Si exhibit smaller magnetization; however, they retain their ferromagnetic ordering for higher temperatures (see Tab. 5.2). LSMO films on NS/Si show a discernible difference in magnetization between the two samples. This may in part be due to the error in thickness determination. Weaker magnetization of the NS/Si samples may also be in part due to normalization to volume as the 90 % NS coverage of the Si substrate has not been taken into account. It is hard to draw any conclusions about the quality and presence of LSMO in gaps between the NS.

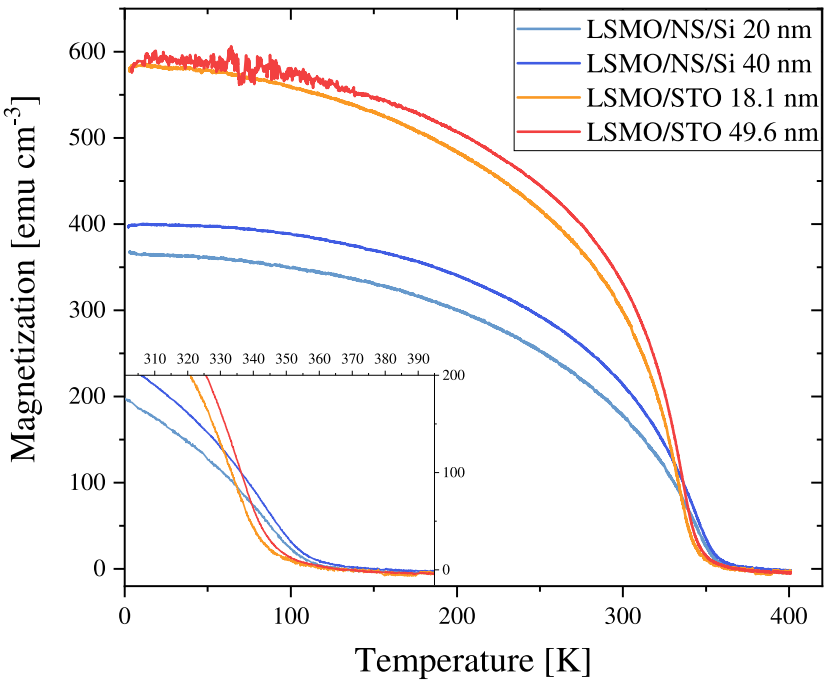

Figure 5.6: Magnetization of LSMO thin films for applied in-plane field of 0.2T.

Sample	LSMO/STO	LSMO/STO	LSMO/NS/Si	LSMO/NS/Si
Thickness [nm]	18.1	49.6	24.1	47.0
T_c [K]	345	347	357	358

Table 5.2: Curie temperature of LSMO samples deposited on STO and NS/Si. Thicknesses of samples deposited on NS/Si have been taken from ellipsometric measurements.

Magnetization hysteresis loops measured at 300 K and 3 K can be seen in Fig. 5.7. Diamagnetic contributions of the STO and Si substrates have been subtracted. The thicker LSMO/STO sample has not been measured at 3 K due to contact of the measurement straw with the inner part of the superconducting coil, which induced additional error for low-temperature measurements (see Fig. 5.6). All samples reach saturation of magnetization for minimal external field, suggesting the easy axis is parallel to the applied field. This behaviour is well documented for LSMO/STO samples where both in-plane directions are equivalent easy axes of magnetization at room temperature. Bellow 250 K the [110] in-plane direction becomes magnetically softer [26]. Samples deposited on NS/Si exhibit substantial hysteresis loop broadening at low temperatures. The cause of this broadening is very interesting and incites future research.

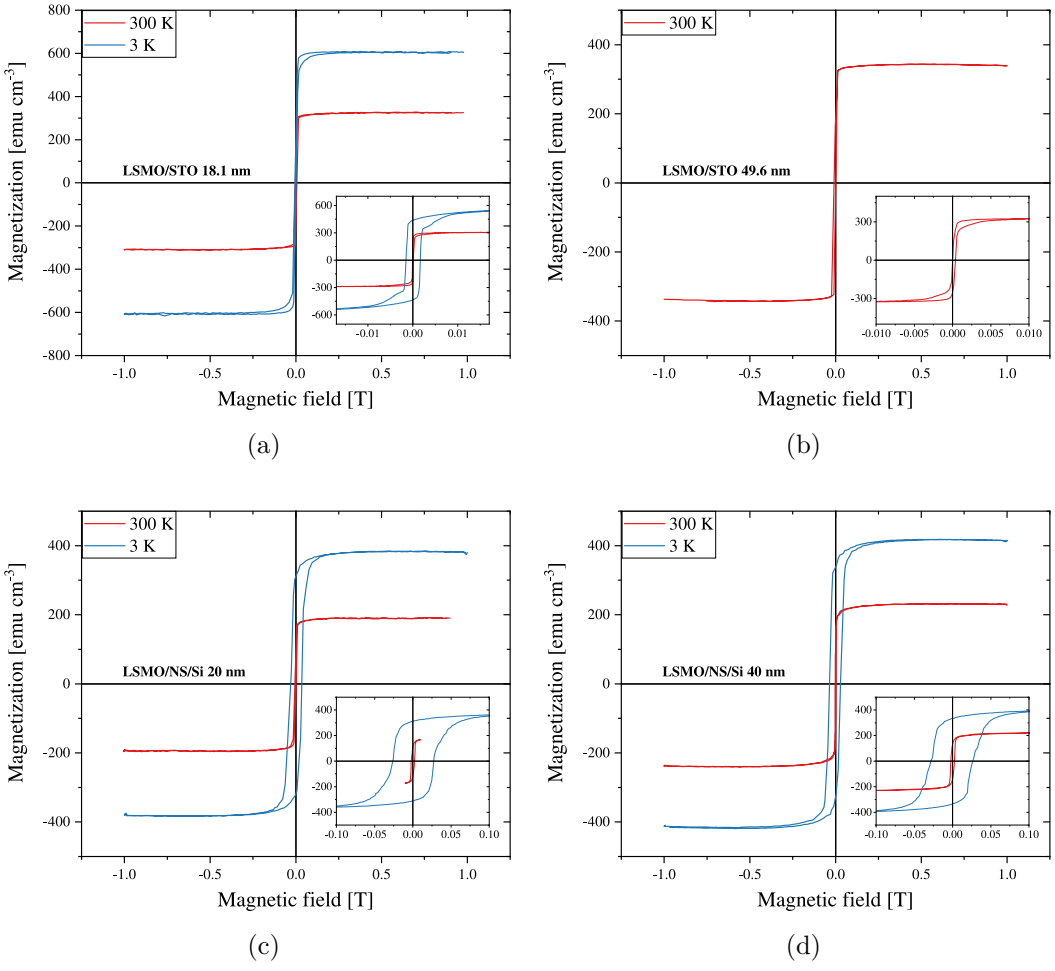

Figure 5.7: Magnetization hysteresis loops of LSMO deposited on STO and NS/Si with applied in-plane external field. Diamagnetic contributions of the STO and Si substrates have been subtracted.

5.5 Optical response

The optical response of the samples has been measured using a Woollam RC2 ellipsometer. Measurements have been carried out for five angles of incidence (55°. 60°, 65°, 70° and 75°) from 0.7 eV to 6.4 eV.

In order to model the optical constants of the thin films, the optical constants of the substrates had to be measured. Spectral dependence of the optical properties of the STO substrate has been determined using a B-spline fit (definition of a B-spline can be found in [31]) of a substrate only measurement (see inset graph in Fig. 5.8). To determine the optical properties of the NS/Si stack, the Si substrate has been measured without the NS. Its optical properties have been found to precisely follow literature (see inset graph in Fig. 5.9) [32]. An approximately 1.5 nm layer of natural oxide, with optical properties taken from [32], has been discovered on the Si surface. Measurement of the NS/Si stack then allowed for the optical characterization of NS using a low-resolution B-spline model.

The diagonal elements of the permittivity tensors of LSMO thin films deposited on STO (as determined by a B-spline model) can be seen in Fig. 5.8. All samples have a similar spectral shape with one distinction around 4 eV. With increasing thickness the double peak in the imaginary part merges into a single peak. This change in the optical properties is likely due to microscopic strain relaxation. That is in agreement with spectroscopic ellipsometry in literature [33], where samples of LSMO grown on a $(LaAlO_3)_{1/3}(Sr_2AlTaO_6)_{2/3}$ substrate with lower epitaxial strain exhibit only one peak in the spectra around this energy.

The optical response of the LSMO samples deposited on NS/Si can be seen in Fig. 5.9. The numerical model used only a B-spline to fit the experimental data. More complicated models, given the textured column growth of LSMO, have been tried (e.g., the effective medium approximation with 90% fill-factor); however, none of them yielded results significantly differing from a B-spline fit and introduced additional fitting parameters and sometimes produced non-physical results. The thickness of the samples (a fitted parameter) has been ascertained as $t_{20} = 24.07$ nm and $t_{40} = 46.95$ nm. The overall spectral shape of the diagonal element of the permittivity tensor somewhat resembles that of the LSMO samples on STO, with a peak around 4 eV in the imaginary part of ε_1 and both real and imaginary parts trailing of in the infra-red region. However, additional peaks are visible at lower energies. The spectra have not been fitted using Lorentz oscillators, which would help with the analysis, as the main focus of this work are the magneto-optical properties of the samples. The changes in the spectra, and most notably the changes between the two LSMO/NS/Si samples, are interesting and worth further inquiry. One explanation of the deviation in the optical response could be the potentialy different stoichiometry of the samples. Additional measurements need to be conducted to validate this claim.

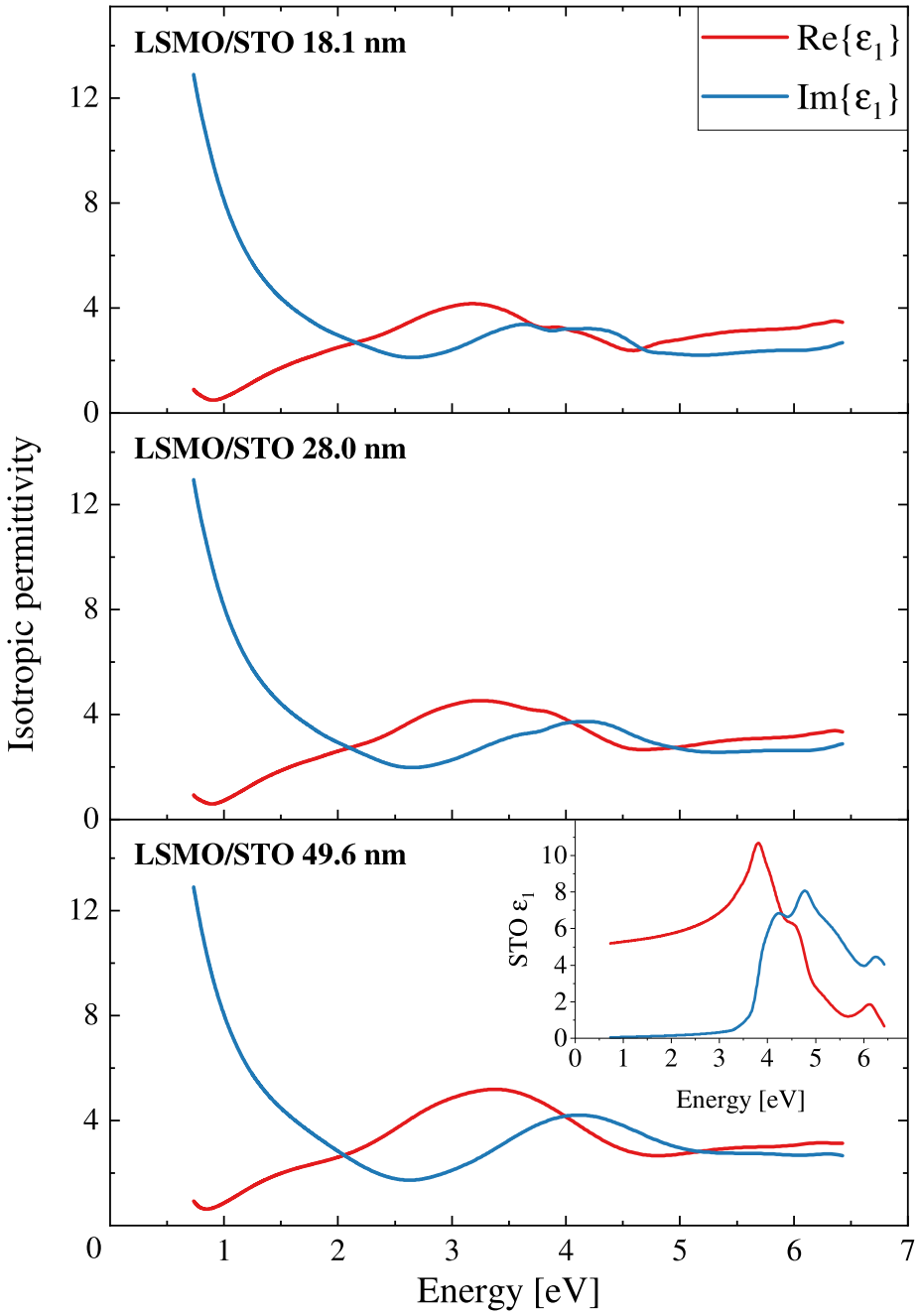

Figure 5.8: Diagonal element of the permittivity tensor of three LSMO/STO samples with differing thicknesses of LSMO numerically modeled by a B-spline. An inset graph shows the optical response of the STO substrate.

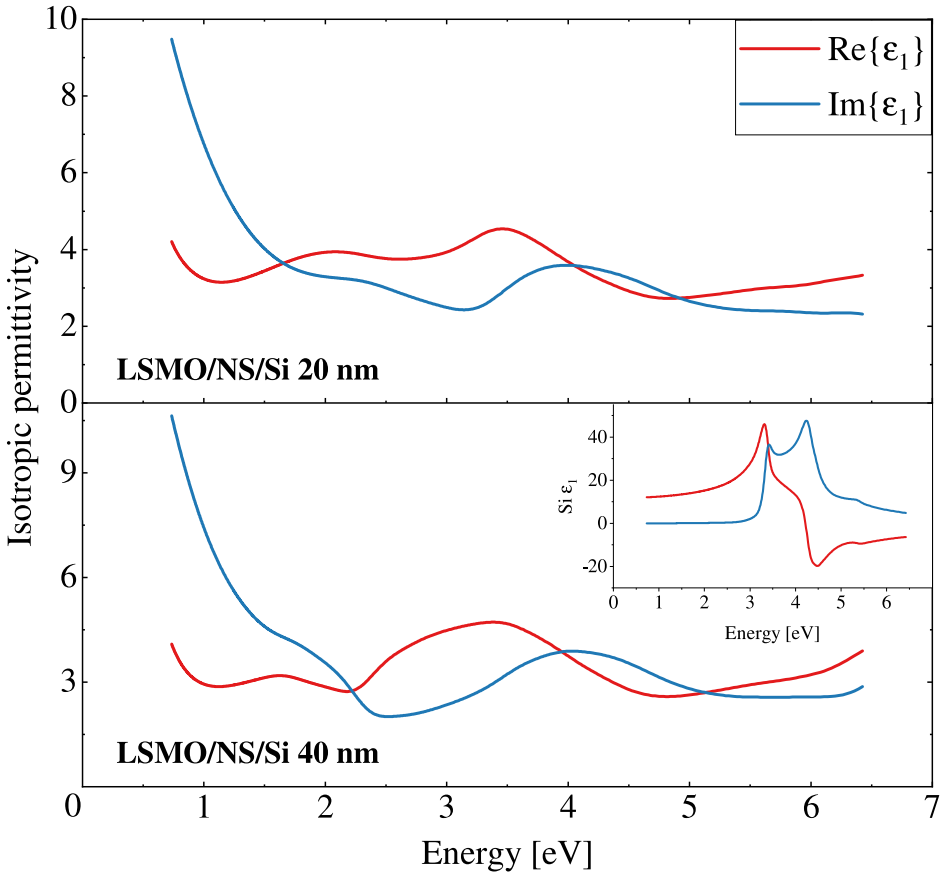

Figure 5.9: Diagonal element of the permittivity tensor of two samples of LSMO on a NS/Si substrate with different thickness of the deposited layer as modeled by a B-spline. The inset graph shows the optical constants of Si taken from [32].

5.6 Magneto-optical response

Magneto-optical response of the samples has been measured using a custom rotating analyser MOKE measurement setup in polar configuration.

In order to determine the external field necessary for polar MOKE measurement in saturation (magnetization loops in Section 5.4 have been measured in the in-plane geometry), Kerr rotation hysteresis loops have been measured for four samples (see Fig. 5.10 and 5.11). Measured MOKE hysteresis loops exhibit much larger saturation fields contrary to the in-plane magnetization loops (see Section 5.4). This suggests that the easy axis of magnetization lies within the plane of the sample, which has already been reported in literature for samples deposited on STO [26].

MOKE spectra, measured at 1 T ensuring a magnetically saturated state, of LSMO deposited on STO are shown in Fig. 5.12. Proper analysis of magnetically active transitions can not be made using only magneto-optical spectra and can be seen in Section 5.7. Nonetheless, from the magneto-optical spectra we can see that the response of all three samples of LSMO deposited on STO is clearly dominated by a spectroscopic structure at around 3.5 eV. This is in agreement with literature [33, 34, 35]. However, in Kerr rotation a double peak is observed around this energy. That is due to the optical influence of STO (see Fig. 5.8), which changes

optical properties substantially in this spectral region. This influence diminishes with increasing thickness as less light penetrates the sample and reflects at the interface of LSMO and STO.

Magneto-optical response of the LSMO/NS/Si samples can be seen in Fig. 5.13. The spectra are again dominated by one spectroscopic structure; however, this time the central energy of the structure differs for both samples. This is due to the optical influence of the substrate, which for these samples is silicon. The reflectivity of silicon increases dramatically around 3.2 eV which again complicates the analysis of these spectra. LSMO thin films are highly transparent in this region, and especially the thinner sample is strongly influenced by the optical response of the substrate.

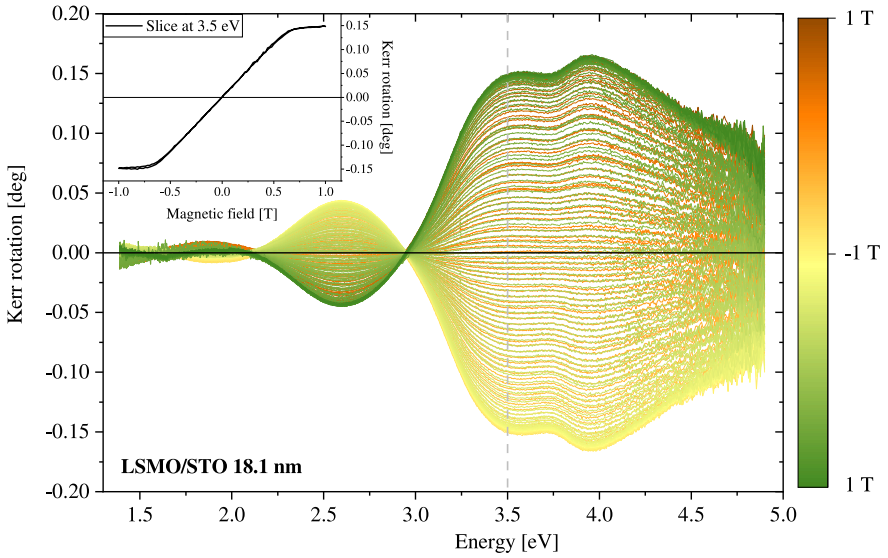

(a)

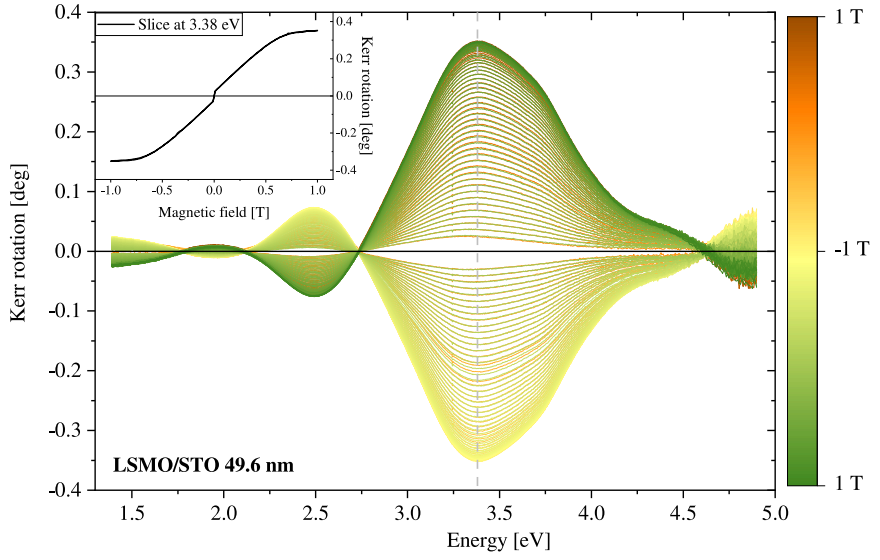

(b)

Figure 5.10: Magneto-optical hysteresis loops of LSMO films of thicknesses (a) 18.1 nm and (b) 49.6 nm deposited on STO. Inset graph represents a slice through the spectra at a given energy.

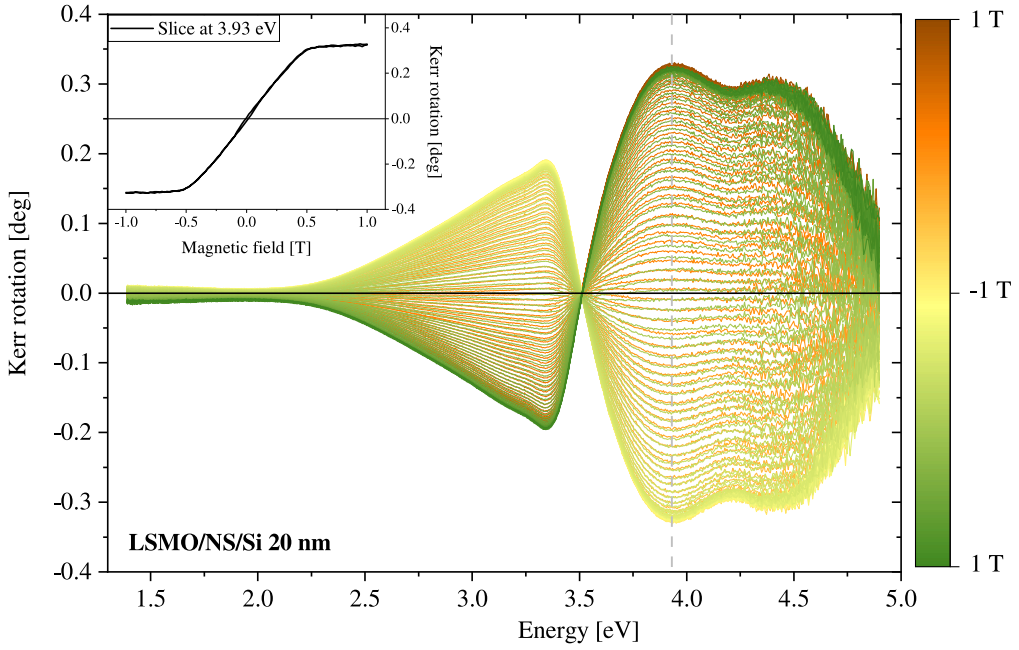

(a)

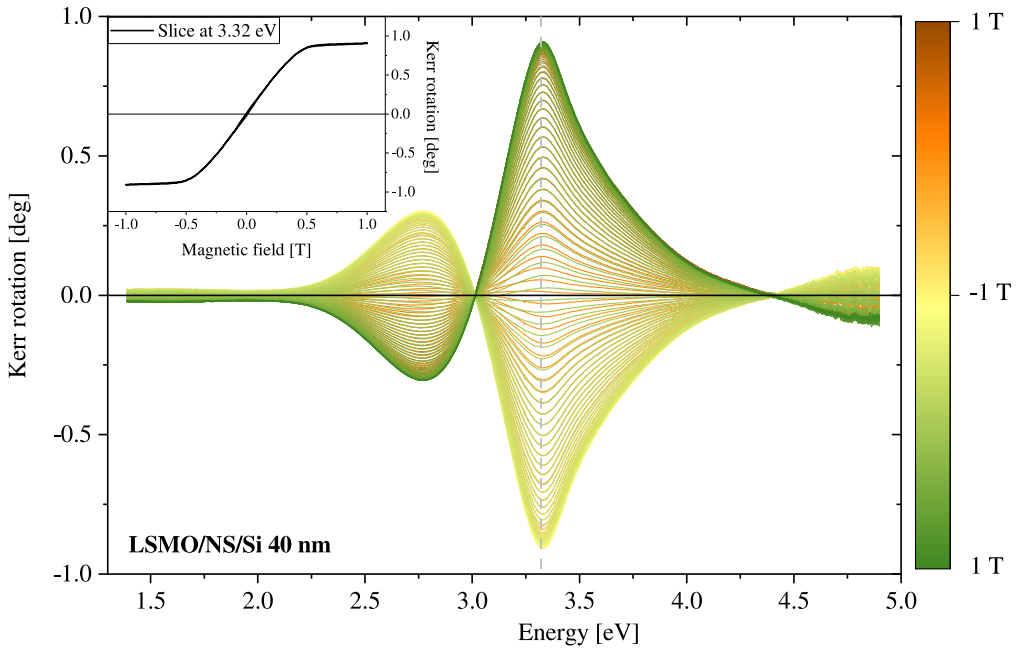

(b)

Figure 5.11: Magneto-optical hysteresis loops of LSMO films of thicknesses (a) 20 nm and (b) 40 nm deposited on NS/Si. Inset graph represents a slice through the spectra at a given energy.

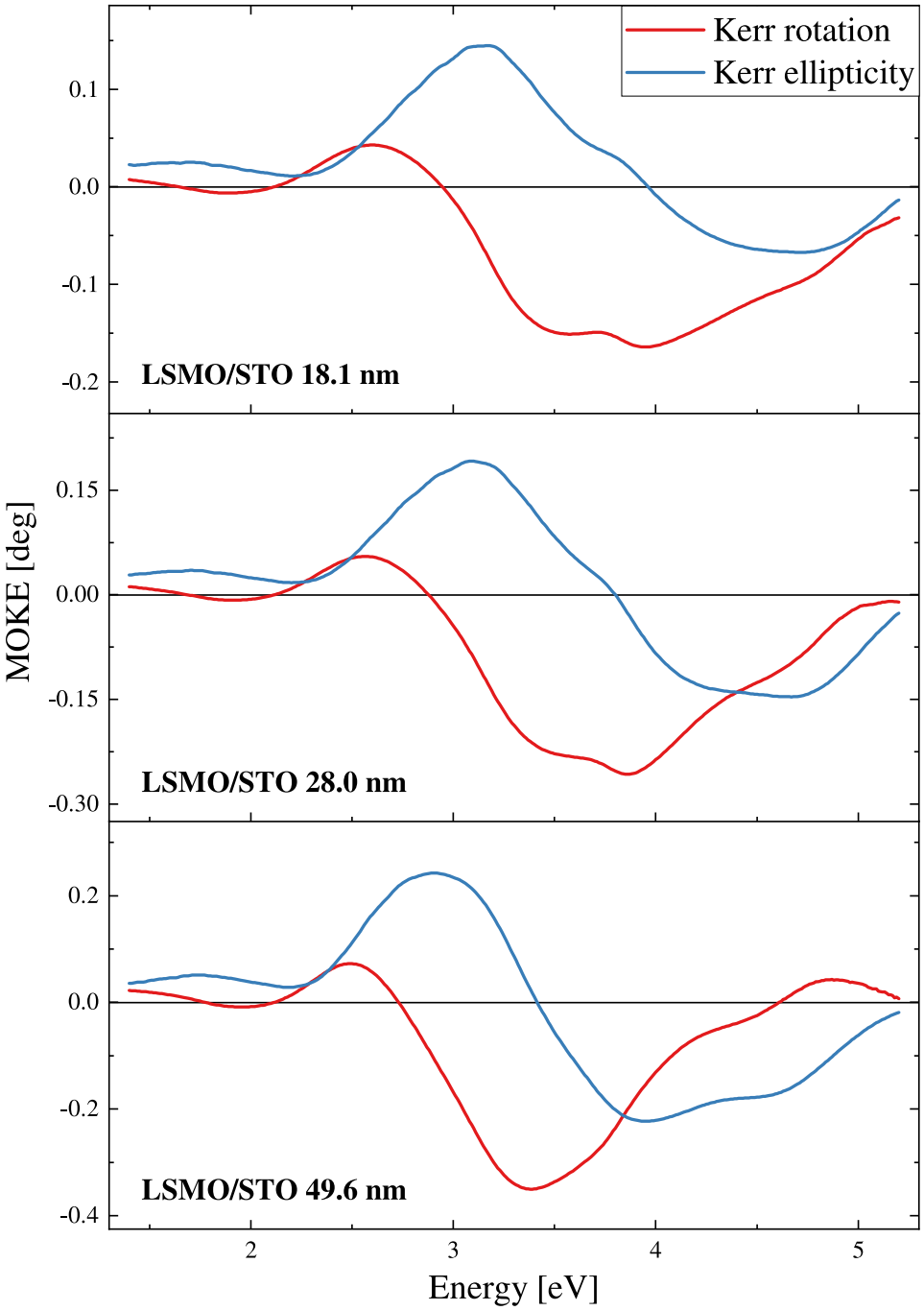

Figure 5.12: Magneto-optical Kerr effect of LSMO layers deposited on STO.

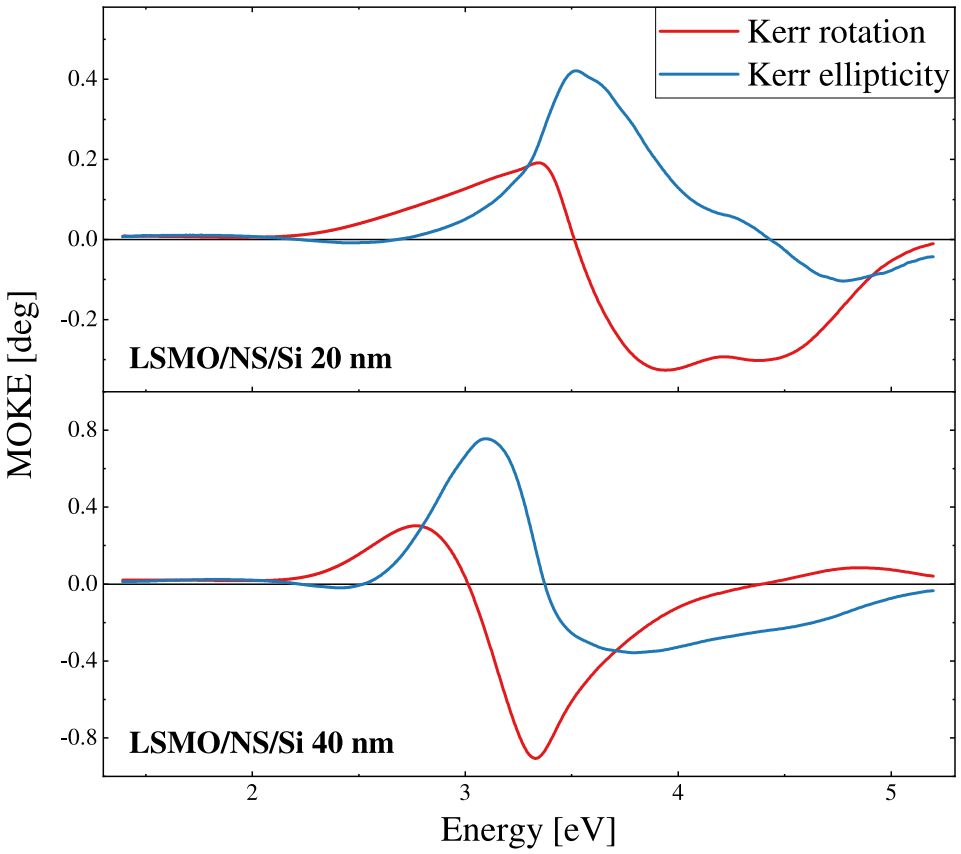

Figure 5.13: Magneto-optical Kerr effect of LSMO layers deposited on NS/Si.

5.7 Magnetically active transitions

Experimental results obtained in the previous sections were used to numerically calculate the spectral dependence of the off-diagonal element of the permittivity tensor. This has been done using Yeh formalism introduced in Section 1.6.

Calculated spectra for the three samples of LSMO on STO and two samples of LSMO on NS/Si can be seen in Fig. 5.14. Little change can be observed for the two thinner (18 nm and 28 nm) samples deposited on STO apart from the slightly lower amplitude of the 28 nm sample. The main spectral structure of the thickest 50 nm sample of LSMO on STO seems to have shifted slightly to higher energies. This supports the earlier narrative of microscopic strain relaxation with increasing thickness of the LSMO layer.

Samples of LSMO deposited on NS/Si display large differences in amplitude of the off-diagonal element of the permittivity tensor. The thicker 40 nm sample displays properties in agreement with magnetization measurements (see Fig. 5.6) as it exhibits lower overall amplitude. However, the thinner 20 nm sample has the largest effect of all samples in contrast to magnetization measurements. As discussed in Section 5.5 this may be in part due to slightly different stoichiometry of the samples, but more experiments, confirming the variation of composition across the samples, are necessary to validate this claim. Important to note is also the large dependency of the off-diagonal element of the permittivity tensor on the diagonal element during the calculation, especially for the thinner sample.

Spectral dependencies of the off-diagonal elements of the permittivity tensors of all samples have been fitted with magneto-optical transitions introduced in Section 1.5. Three diamagnetic transitions have been found to fit all samples adequately. Their fitted parameters can be seen in Table 5.3. The fitted spectra can also be seen in Figs. 5.15 and 5.16. The dominating diamagnetic transition at around 3.5 eV has already been reported in literature [33, 36] as a charge transfer transition from O $2p$ states into Mn t_{2g} states in the minority spin channel. Spectral features around 2.4 eV have been previously explained in literature [36] by a large diamagnetic transition at 1.2 eV or using a paramagnetic transition at 2.4 eV [33]. Neither of these approaches describes our data adequately. As such, we propose two diamagnetic transitions located at around 1.9 eV and 2.9 eV. These transitions fit the off-diagonal elements of the permittivity tensor well in a wide spectral region. Partial density of states calculations taken from the literature have been consulted regarding the validity of these transitions [34]. Both transitions have been ascribed to charge transfer transitions from O $2p$ to Mn t_{2g} states in the majority spin channel.

The ε_2 spectra in Figs. 5.15 and 5.16 all show deviation from their respective fits in the UV region. This deviation can be severely mitigated by adding a diamagnetic transition at around 5.5 eV corresponding to a charge transfer transition from an O $2p$ state to a Mn t_{2g} state in the minority spin channel, which was taken into account based on literature [34]. However, as this transition is beyond our measured spectral region, it has not been included in the fit. A broader spectral region would have to be measured to fully justify this claim.

Substrate	STO	STO	STO	Si/NS	Si/NS
Thickness [nm]	18.1	28.0	49.6	20	40
Transition 1	Charge transfer transition O $2p \rightarrow$ Mn t_{2g} in the majority spin channel				
$(\varepsilon_2')_{max}$	0.009	0.009	0.009	0.007	0.007
E_0 [eV]	1.9	1.9	1.9	2.04	1.98
Γ [eV]	0.69	0.68	0.67	0.76	0.64
Transition 2	Charge transfer transition O $2p \rightarrow$ Mn t_{2g} in the majority spin channel				
$(\varepsilon_2')_{max}$	-0.018	-0.019	-0.025	-0.023	-0.016
E_0 [eV]	2.88	2.86	2.95	2.82	2.74
Γ [eV]	0.8	0.79	0.86	0.79	0.84
Transition 3	Charge transfer transition O $2p \rightarrow$ Mn t_{2g} in the minority spin channel				
$(\varepsilon_2')_{max}$	0.055	0.051	0.058	0.066	0.042
E_0 [eV]	3.5	3.5	3.53	3.52	3.51
Γ [eV]	0.99	1.06	1.12	0.85	1.1

Table 5.3: Parameters of the transitions used to describe spectra of the off-diagonal element of the permittivity tensor of LSMO thin films of different thicknesses on two different substrates. All three transitions are diamagnetic with maximum amplitude of the real part $(\varepsilon_2')_{max}$, resonant frequency E_0 and spectral broadening of the oscillators Γ.

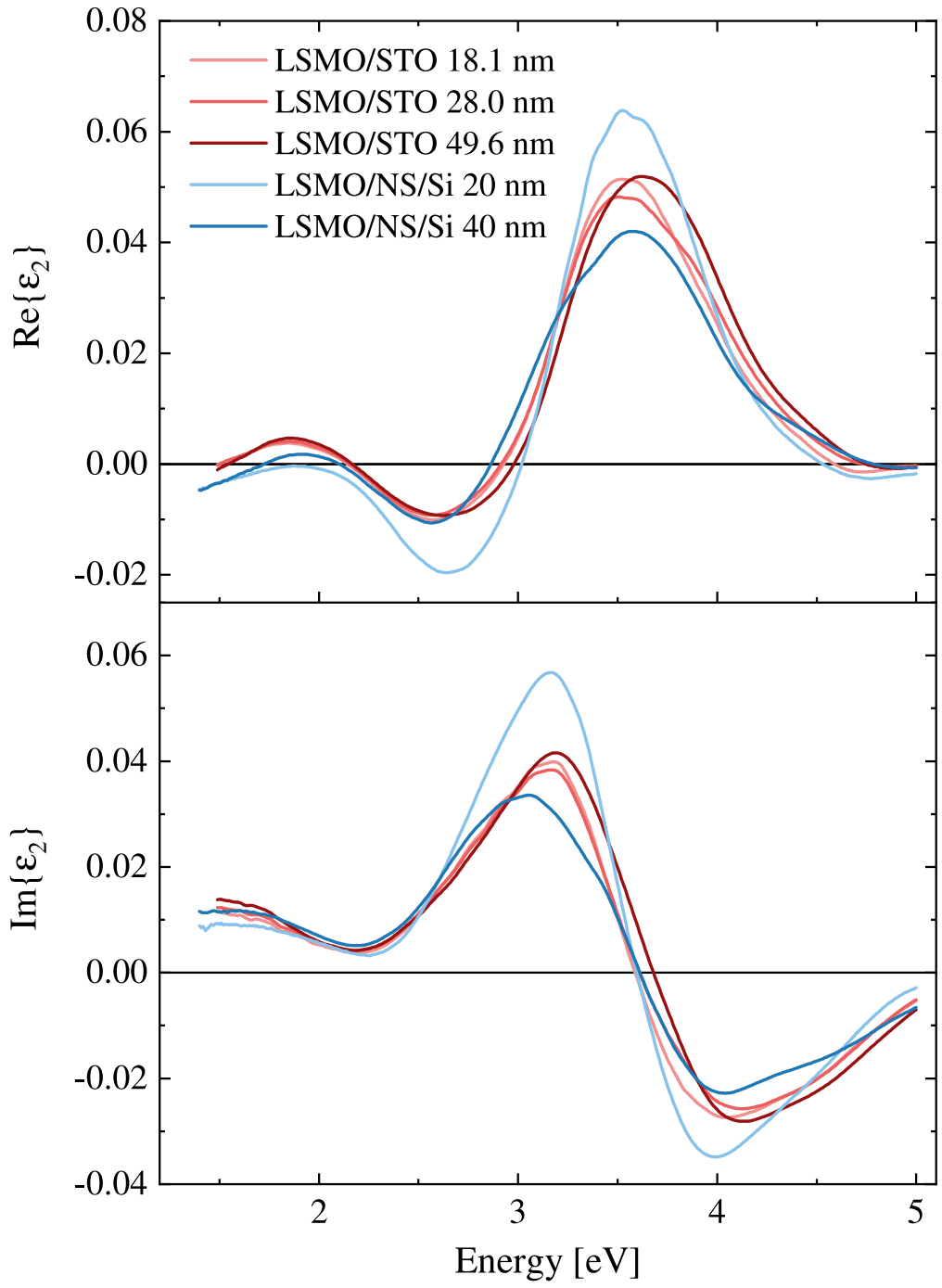

Figure 5.14: Off-diagonal elements of the permittivity tensor of LSMO films with varying thickness deposited on two different substrates. The spectra of ε_2 have been numerically calculated using Yeh formalism.

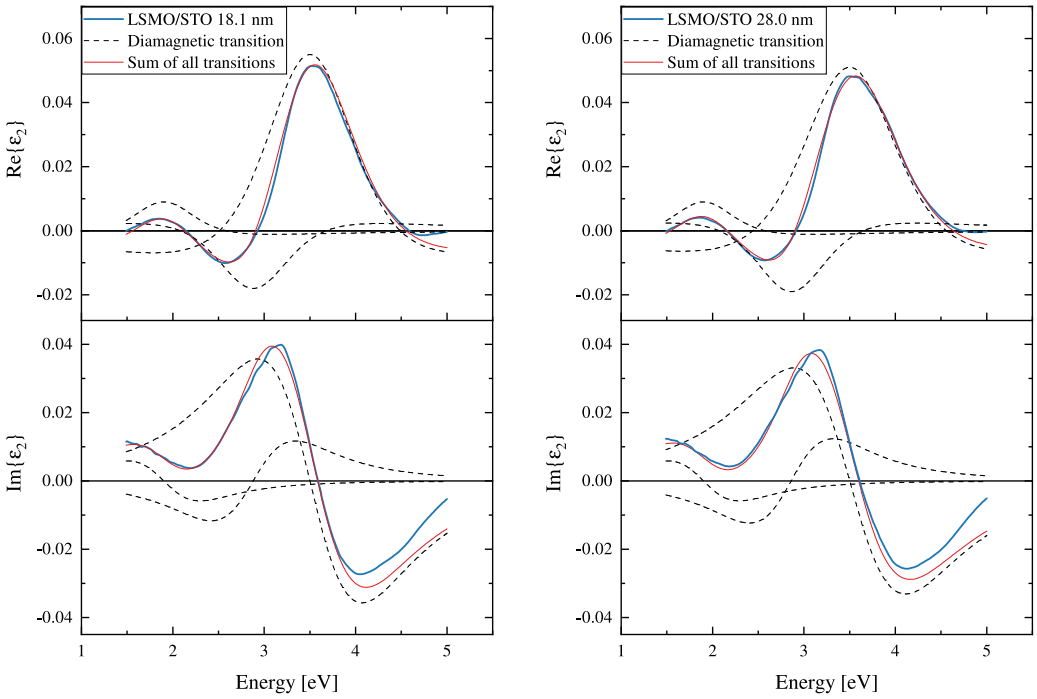

(a)

(b)

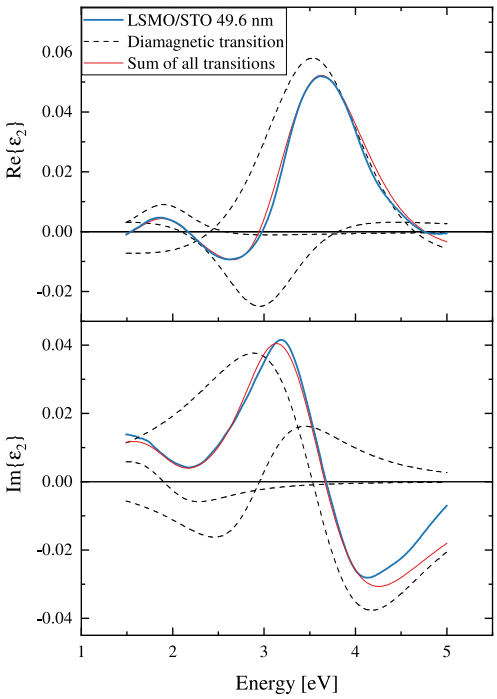

(c)

Figure 5.15: Parameterised spectra of the off-diagonal element of the permittivity tensor of an (a) 18.1 nm, (b) 28.0 nm and (c) 49.6 nm thick film of LSMO on STO. Parameters of the diamagnetic transitions can be seen in Table 5.3.

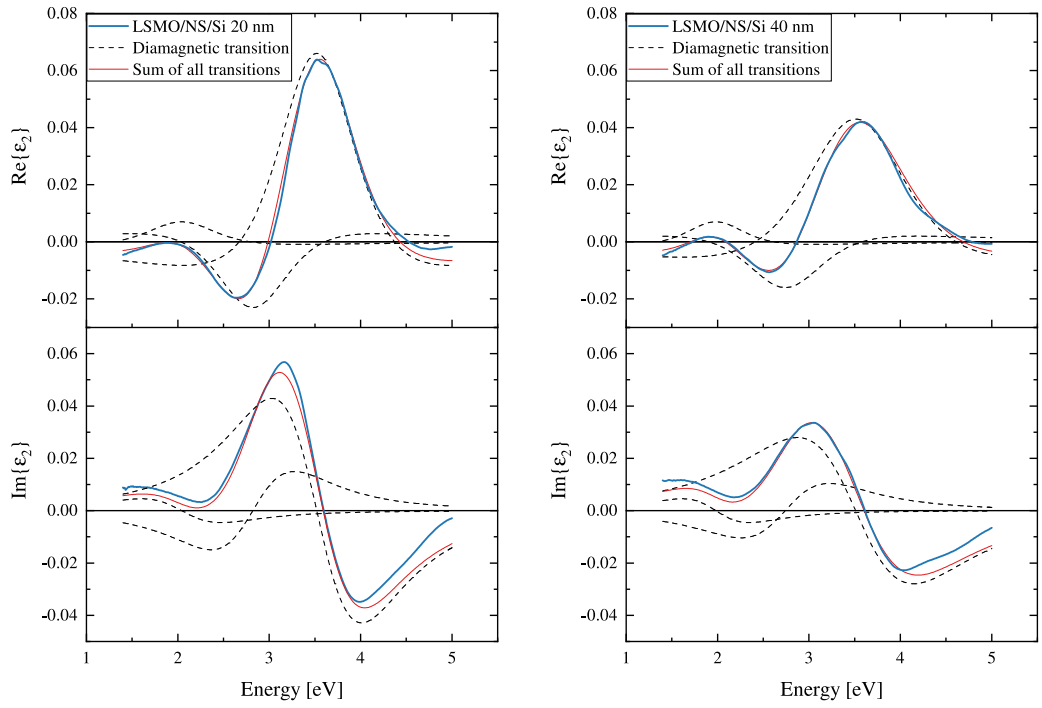

(a) (b)

Figure 5.16: Parameterised spectra of the off-diagonal element of the permittivity tensor of an (a) 20 nm and (b) 40 nm thick film of LSMO on the NS/Si stack. Parameters of the diamagnetic transitions can be seen in Table 5.3.

5.8 Temperature-dependent properties

Optical and magneto-optical properties of an 18 nm thick sample of LSMO on STO have been examined from 300 K to 350 K. Numerical calculation of the full permittivity tensor has been carried out.

5.8.1 Spectroscopic ellipsometry

Temperature-dependent spectroscopic ellipsometry setup has been constructed using a combination of an ARS DE-204 cryostat and a Woollam RC2 ellipsometer. This setup allows for spectroscopic ellipsometry measurements from 4 K to 800 K. The angle of incidence is fixed at 70°.

The optical response of the substrate, used to model the permittivity of thin film LSMO, has been measured from 300 K to 350 K. No significant change in optical properties has been observed for this range of temperatures. However, due to a single angle measurement and the introduction of additional optical components (cryostat windows), the resulting model of the permittivity of STO exhibited error larger than the temperature change. This is not surprising as the same error is observed when one tries to fit the data acquired by an ellipsometer at a single angle of incidence. Therefore the optical properties of STO acquired at room temperature (see Fig. 5.8) have been used to model the temperature-dependent optical response of LSMO.

The diagonal element of the permittivity tensor of thin film LSMO deposited on STO, modeled from the measured optical response by a B-spline fit, can be seen in Fig. 5.17. Notable temperature dependence in the real part of diagonal permittivity can be observed for low photon energies. As LSMO is a half-metal, acting as a metal for one orientation of spin and as an insulator for the other, this change is likely due to the thermal excitation of free electrons.

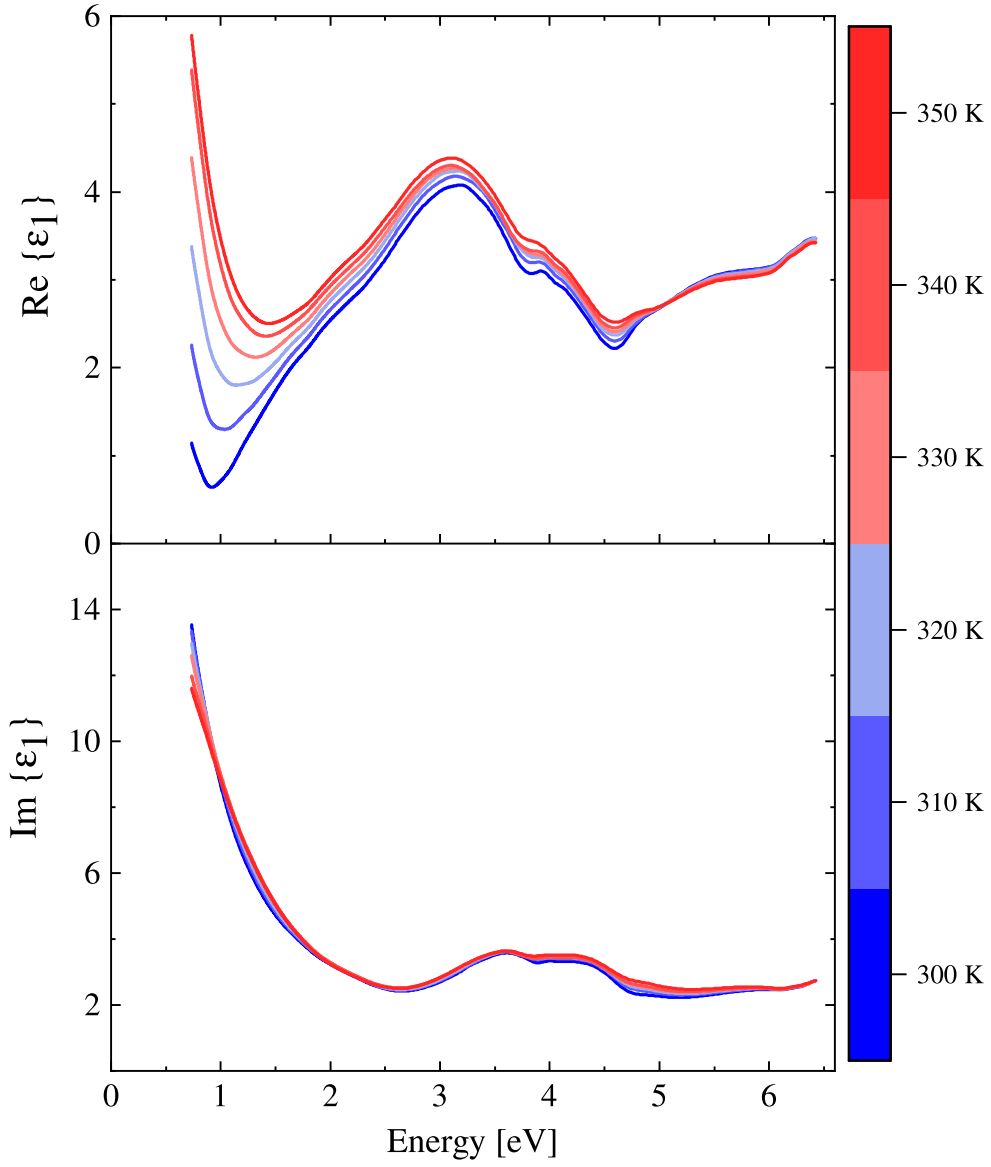

Figure 5.17: Diagonal element of the permittivity tensor of an 18.1 nm thick LSMO film deposited on STO for temperatures between 300 K and 350 K. Observed change in the infrared region is likely due to thermal excitation of free electrons.

5.8.2 Magneto-optical spectroscopy

A custom magneto-optical spectroscopy setup has been constructed around a Montana s50 Cryostation with possible MOKE measurements for temperatures ranging from 4 K to 350 K.

The entry aperture of the cryostat does not allow for spacial separation of the incident and reflected light beams. Hence, a perfect normal incidence setup with a beam splitter has been constructed. Measuring the change in polarization for a wide spectral region (1.4 eV to 4.3 eV) puts a lot of constraints on the quality of the beam splitter. In order to mitigate the influence of the beam splitter on the measured polarization state, a HOMOSIL quartz window has been used at a low angle of incidence. Whilst lowering the detected intensity significantly at a low angle of incidence, the effect on the measured polarization state is negligible.

Faraday effect of the cryostat window has been subtracted from the measured data. This has been achieved by measuring the Faraday effect with a non-magnetic mirror in place of the sample.

Temperature dependence of magneto-optical Kerr effect of LSMO deposited on STO can be seen in Fig. 5.18 for temperatures between 300 K and 350 K. Lowering of the overall amplitude of the MOKE signal is observed as Curie temperature is being approached.

5.8.3 Magnetically active transitions

The spectral dependence of the off-diagonal element of the permittivity tensor has been numerically calculated using Yeh formalism for all temperatures (see Fig. 5.19). The resulting spectra scale strongly with temperature as Curie temperature is being approached (see Table 5.2). However, the non-zero amplitude of the 350 K measurement (i.e., above T_c) was observed. This is given by the nature of Curie temperature measurement in Section 5.4. Magnetometry measurements are more sensitive to long-range magnetic ordering, whereas magneto-optical measurements are also sensitive to short-range magnetic ordering, which can persist above the Curie temperature [37].

Spectra of the off-diagonal element of the permittivity tensor have been fitted with magneto-optical transitions (see Table 5.4). All transitions scale in magnitude with temperature. The broadening of all transitions stays almost constant; however, it differs slightly from that measured at room temperature. The cause of this is the lower precision of the temperature-dependent measurements. Nonetheless, apart from the first transition at around 1.9 eV this change is negligible. The change for the first transition is given by its low amplitude and hence higher error in the determination of its spectral broadening. Not to mention the possible influence of transitions beyond our measured spectral region. Interestingly the resonant frequency of the largest diamagnetic transition at 3.5 eV starts shifting to higher energies with rising temperature. This is likely the effect of strain modification in the thin film as the crystal lattice of the substrate STO expands at a different rate than that of LSMO [38].

For high-temperature measurements a constant offset of the spectra of the imaginary part of ε_2 is observed. This offset is discernible for the 340 K and 350 K measurements. As such, it is probably connected to the transition between the ferromagnetic and paramagnetic states around these temperatures. Unfortu-

nately, a more concrete explanation of this offset can not be provided as of the writing of this thesis.

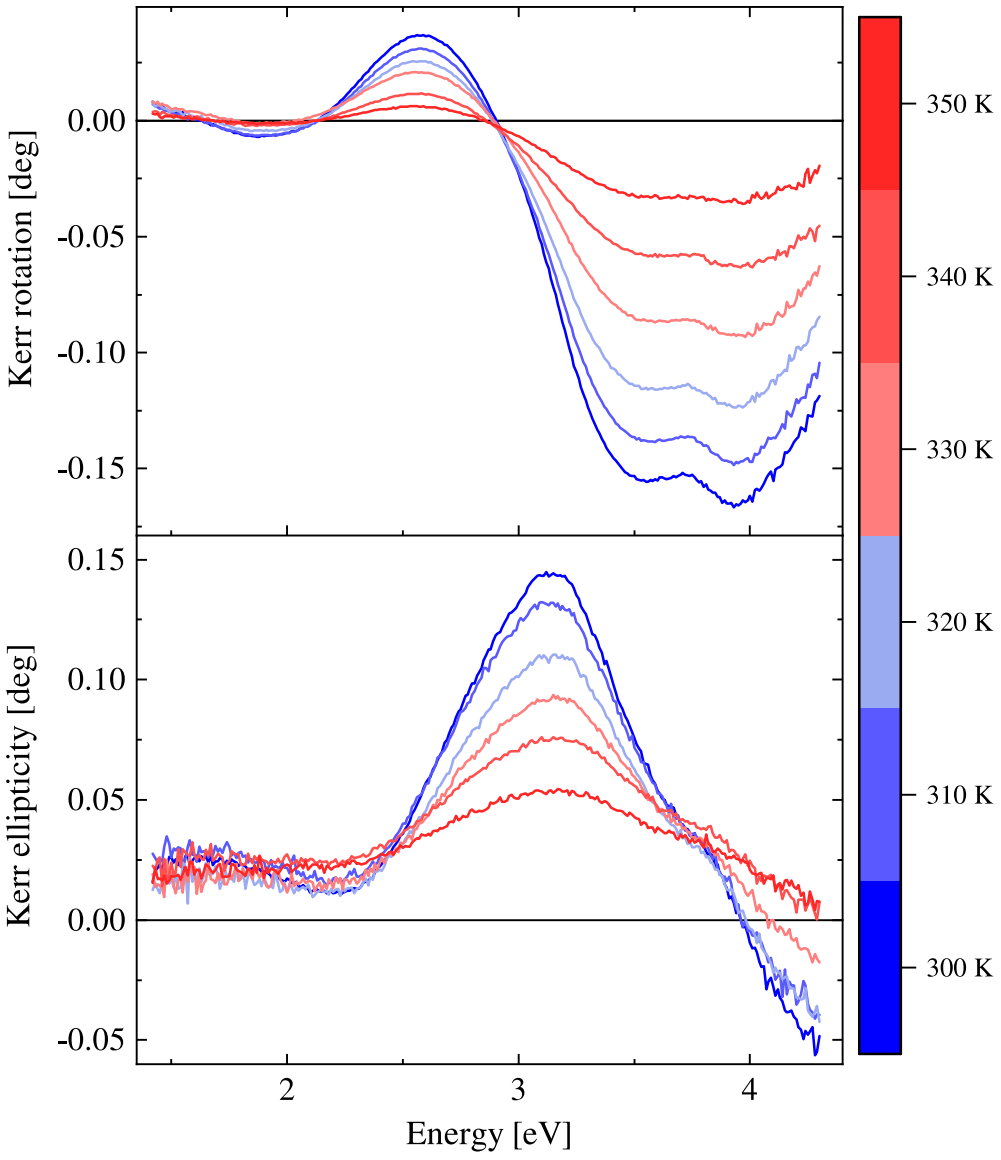

Figure 5.18: Temperature dependent magneto-optical measurement of an 18.1 nm thick LSMO layer deposited on STO. Rapid drop of MOKE signal is observed as Curie temperature is approached.

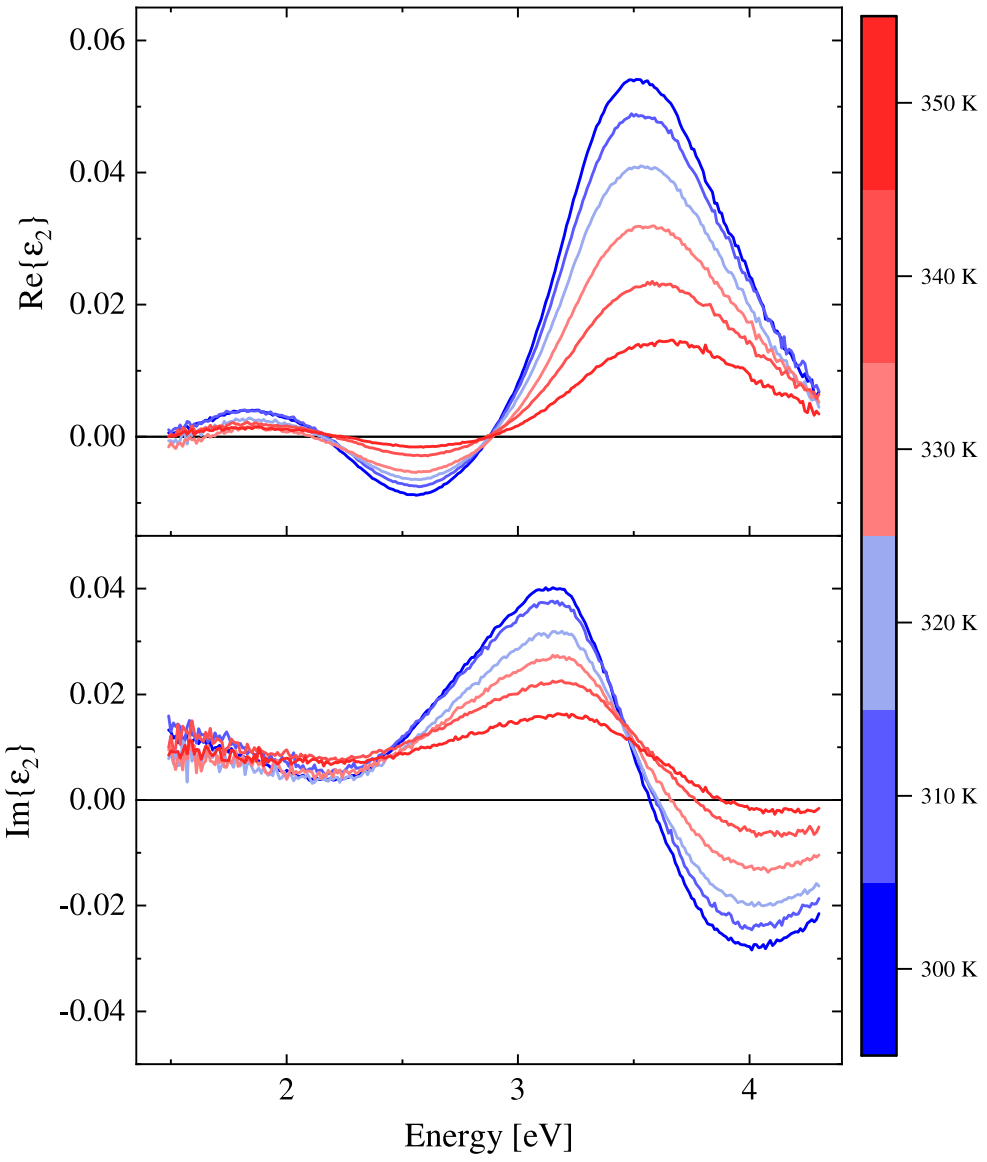

Figure 5.19: Temperature dependent spectra of the off-diagonal element of the permittivity tensor of an 18.1 nm thick LSMO film on top of STO.

Temperature [K]	300	310	320	330	340	350
Transition 1	Charge transfer transition O $2p \rightarrow$ Mn t_{2g} in the majority spin channel					
$(\varepsilon_2')_{max}$	0.01	0.009	0.008	0.005	0.004	0.003
E_0 [eV]	1.9	1.9	1.9	1.9	1.9	1.9
Γ [eV]	0.76	0.76	0.76	0.76	0.76	0.76
Transition 2	Charge transfer transition O $2p \rightarrow$ Mn t_{2g} in the majority spin channel					
$(\varepsilon_2')_{max}$	-0.015	-0.013	-0.011	-0.009	-0.004	-0.003
E_0 [eV]	2.88	2.88	2.88	2.88	2.88	2.88
Γ [eV]	0.84	0.84	0.84	0.84	0.84	0.84
Transition 3	Charge transfer transition O $2p \rightarrow$ Mn t_{2g} in the minority spin channel					
$(\varepsilon_2')_{max}$	0.058	0.052	0.043	0.034	0.024	0.015
E_0 [eV]	3.5	3.5	3.51	3.52	3.56	3.58
Γ [eV]	0.96	0.96	0.96	0.96	0.94	0.96

Table 5.4: Parameters of the MO transitions used to describe spectra of the off-diagonal element of the permittivity tensor of 18.1 nm thick LSMO/STO sample for different temperatures. All three transitions are diamagnetic with maximum amplitude of the real part $(\varepsilon_2')_{max}$, resonant frequency E_0 and spectral broadening of the oscillators Γ.

Conclusion

A comprehensive study of LSMO thin films deposited on silicon with the aid of a NS seed layer has been presented. Epitaxial films of LSMO atop STO have been used for comparison.

Pulsed laser deposition and oxygen annealing have been employed for the growth of LSMO films. Three samples of LSMO have been deposited on STO with thicknesses of 18.1 nm, 28.0 nm, and 49.6 nm. Atop the NS/Si substrate two samples were deposited with thicknesses of 24 nm and 47 nm. Subsequent AFM and XRD measurements revealed good epitaxial growth of LSMO on STO as well as the presence of unstrained LSMO on top of NS/Si. Magnetometry measurements revealed lower overall magnetization of the samples deposited on NS/Si; however, Curie temperatures for these samples were 11 K higher on average. Hysteresis curve measurements suggest the easy axis lies in-plane of the film for all samples, with interesting loop broadening for LSMO/NS/Si samples at lower temperatures.

Optical measurements revealed only small changes in optical properties for samples of LSMO atop STO. Larger differences in optical properties have been observed for the LSMO thin films on NS/Si. The origin of these differences has not been concluded; however, the theory of a change in stochiometry between the samples has been proposed. Optical measurements have also been used to determine the film thickness of samples grown on silicon. Magneto-optical measurements have been carried out with subsequent numerical calculations of the off-diagonal element of the permittivity tensor. Spectra of the off-diagonal element of samples grown on STO showed negligible changes apart from the slight shift of the largest transition to higher energies for the thickest sample. The origin of this shift lies in microscopic strain relaxation. The thicker sample of LSMO on NS/Si showed a lower overall amplitude of the spectral dependence of the off-diagonal element of the permittivity tensor in agreement with magnetization measurements. On the contrary, the thinner sample of LSMO on NS/Si exhibited a greater amplitude of the spectral dependence of the off-diagonal element of the permittivity tensor than all the other samples. This is in stark contrast to magnetization measurements. Our explanation so far is the aforementioned difference in stochiometry; however, further research is necessary for a full explanation of this phenomenon. Spectra of the off-diagonal element of the permittivity tensor have been fitted for all samples by three diamagnetic transitions at around 1.9, 2.9, and 3.5 eV. The transition at 3.5 eV has already been reported in the literature as a charge transfer transition from an O $2p$ state to a Mn t_{2g} state in the minority spin channel. Two other transitions, not previously reported in the literature, have been used to explain the spectral shape at lower energies. Both transitions originate in the majority spin channel in a charge transfer transition between the O $2p$ and Mn t_{2g} state.

Setups for optical and magneto-optical measurements with varying temperatures have been constructed. The thinnest sample of LSMO on STO has been examined for temperatures between 300 K and 350 K. Numerical calculations of the temperature depended off-diagonal element of the permittivity tensor revealed amplitude scaling with temperature. Short-range magnetic ordering allowed for

observation of non-zero amplitude above Curie temperature. Shifting of the diamagnetic transition at 3.5 eV towards higher energies has been observed with increasing temperature as a result of different thermal expansion coefficients of LSMO and STO.

Bibliography

[1] M. Bowen, M. Bibes, A. Barthélémy, et al. Nearly total spin polarization in $La_{2/3}Sr_{1/3}MnO_3$ from tunneling experiments. *Applied Physics Letters*, 82 (2):233–235, jan 2003. doi: 10.1063/1.1534619.

[2] A. P. Ramirez. Colossal magnetoresistance. *Journal of Physics: Condensed Matter*, 9(39):8171–8199, sep 1997. doi: 10.1088/0953-8984/9/39/005.

[3] G.H. Jonker and J.H. Van Santen. Ferromagnetic compounds of manganese with perovskite structure. *Physica*, 16(3):337–349, March 1950. doi: 10.1016/0031-8914(50)90033-4.

[4] C. Zener. Interaction between the d-shells in the transition metals. II. ferromagnetic compounds of manganese with perovskite structure. *Physical Review*, 82(3):403–405, May 1951.

[5] J. M. Vila-Fungueiriño, J. Gázquez, C. Magén, et al. Epitaxial $La_{0.7}Sr_{0.3}MnO_3$ thin films on silicon with excellent magnetic and electric properties by combining physical and chemical methods. *Science and Technology of Advanced Materials*, 19(1):702–710, oct 2018. doi: 10.1080/14686996.2018.1520590.

[6] T. Maleček. *Strain influence on magneto-optical properties of* $La_{2/3}Sr_{1/3}MnO_3$. Bachelor thesis, Prague, June 2020.

[7] L. Motl and M. Zahradník. *Pěstujeme lineární algebru*. Karolinum, Prague, 1995. ISBN 8071841862.

[8] Š. Višňovský. *Optics in magnetic multilayers and nanostructures*. CRC Taylor & Francis, Boca Raton, March 2006. ISBN 9780849336867.

[9] L. Beran. *Optical and magneto-optical studies of ferrimagnetic garnets for photonic and spintronic applications*. PhD thesis, Prague, April 2020.

[10] F. J. Kahn, P. S. Pershan, and J. P. Remeika. Ultraviolet magneto-optical properties of single-crystal orthoferrites, garnets, and other ferric oxide compounds. *Physical Review*, 186(3):891–918, October 1969. doi: 10.1103/physrev.186.891.

[11] P. S. Pershan. Magneto-optical effects. *Journal of Applied Physics*, 38(3): 1482–1490, March 1967. doi: 10.1063/1.1709678.

[12] L.D. Landau and E.M. Lifshitz. *Electrodynamics of Continuous Media*. Pergamon Press, Tarrytown, second edition, 1984. ISBN 9780080302751.

[13] J. M. D. Coey. *Magnetism and magnetic materials*. Cambridge University Press, Cambridge New York, 2009. ISBN 9780511845000.

[14] K. R. Chen, J. N. Leboeuf, R. F. Wood, et al. Mechanisms affecting kinetic energies of laser-ablated materials. *Journal of Vacuum Science & Technology A: Vacuum, Surfaces, and Films*, 14(3):1111–1114, May 1996. doi: 10.1116/1.580278.

[15] W. Prellier, P. Lecoeur, and B. Mercey. Colossal-magnetoresistive manganite thin films. *Journal of Physics: Condensed Matter*, 13(48):R915–R944, November 2001. doi: 10.1088/0953-8984/13/48/201.

[16] S. Daniš. *Atomová fyzika a elektronová struktura látek*. MatfyzPress, Prague, 2019. ISBN 9788073783761.

[17] M. Zahradník. *Dynamic control of magnetization for spintronic applications studied by magneto-optical methods*. PhD thesis, Charles University, Prague, June 2019.

[18] H. Fujiwara. *Spectroscopic Ellipsometry*. Wiley-Blackwell, Hoboken, NJ, January 2007. ISBN 978-0-470-01608-4.

[19] A-M Haghiri-Gosnet and J-P Renard. CMR manganites: physics, thin films and devices. *Journal of Physics D: Applied Physics*, 36(8):R127–R150, April 2003. doi: 10.1088/0022-3727/36/8/201.

[20] A. Vailionis, H. Boschker, W. Siemons, et al. Misfit strain accommodation in epitaxial ABO_3 perovskites: Lattice rotations and lattice modulations. *Physical Review B*, 83(6), February 2011. doi: 10.1103/PhysRevB.83.064101.

[21] M. C. Martin, G. Shirane, Y. Endoh, et al. Magnetism and structural distortion in the $La_{0.7}Sr_{0.3}MnO_3$ metallic ferromagnet. *Physical Review B*, 53 (21):14285–14290, June 1996. doi: 10.1103/physrevb.53.14285.

[22] F. He and B. O. Wells. Lattice strain in epitaxial $BaTiO_3$ thin films. *Applied Physics Letters*, 88(15):152908, April 2006. doi: 10.1063/1.2194231.

[23] A. Boileau, M. Dallocchio, F. Baudouin, et al. Textured manganite films anywhere. *ACS Applied Materials & Interfaces*, 11(40):37302–37312, 2019. doi: 10.1021/acsami.9b12209.

[24] C. Aruta, G. Ghiringhelli, A. Tebano, et al. Strain induced x-ray absorption linear dichroism in $La_{0.7}Sr_{0.3}MnO_3$ thin films. *Physical Review B*, 73(23), June 2006. doi: 10.1103/physrevb.73.235121.

[25] A. Khapikov, L. Uspenskaya, I. Bdikin, et al. Magnetic domains and twin structure of the $La_{0.7}Sr_{0.3}MnO_3$ single crystal. *Applied Physics Letters*, 77 (15):2376–2378, October 2000. doi: https://doi.org/10.1063/1.1316773.

[26] F. Tsui, M. C. Smoak, T. K. Nath, and C. B. Eom. Strain-dependent magnetic phase diagram of epitaxial $La_{0.67}Sr_{0.33}MnO_3$ thin films. *Applied Physics Letters*, 76(17):2421–2423, April 2000. doi: 10.1063/1.126363.

[27] Z. Li, D. Song, R. Yu, et al. Competing interfacial reconstruction mechanisms in $La_{0.7}Sr_{0.3}MnO_3/SrTiO_3$ heterostructures. *ACS Applied Materials &amp Interfaces*, 8(36):24192–24197, September 2016. doi: 10.1021/acsami.6b07569.

[28] X. Li, I. Lindfors-Vrejoiu, M. Ziese, et al. Impact of interfacial coupling of oxygen octahedra on ferromagnetic order in $La_{0.7}Sr_{0.3}MnO_3/SrTiO_3$ heterostructures. *Scientific Reports*, 7(1), January 2017. doi: 10.1038/srep40068.

[29] A. Alberca, C. Munuera, J. Tornos, et al. Ferroelectric substrate effects on the magnetism, magnetotransport, and electroresistance of $La_{0.7}Ca_{0.3}MnO_3$ thin films on $BaTiO_3$. *Physical Review B*, 86(14), October 2012. doi: 10.1103/physrevb.86.144416.

[30] D. Pesquera, X. Marti, V. Holy, et al. X-ray interference effects on the determination of structural data in ultrathin $La_{2/3}Sr_{1/3}MnO_3$ epitaxial thin films. *Applied Physics Letters*, 99(22):221901, November 2011. doi: 10.1063/1.3663574.

[31] J. W. Weber, T. A. R. Hansen, M. C. M. van de Sanden, and R. Engeln. B-spline parametrization of the dielectric function applied to spectroscopic ellipsometry on amorphous carbon. *Journal of Applied Physics*, 106(12):123503, December 2009. doi: 10.1063/1.3257237.

[32] C. M. Herzinger, B. Johs, W. A. McGahan, et al. Ellipsometric determination of optical constants for silicon and thermally grown silicon dioxide via a multi-sample, multi-wavelength, multi-angle investigation. *Journal of Applied Physics*, 83(6):3323–3336, March 1998. doi: 10.1063/1.367101.

[33] M. Zahradník, T. Maroutian, M. Zelený, et al. Electronic structure of $La_{2/3}Sr_{1/3}MnO_3$: Interplay of oxygen octahedra rotations and epitaxial strain. *Physical Review B*, 99(19), May 2019. doi: 10.1103/physrevb.99.195138.

[34] L. Uba, S. Uba, L. P. Germash, et al. Electronic structure and magneto-optical spectra of $La_xSr_{1-x}MnO_3$ perovskites: Theory and experiment. *Physical Review B*, 85(12), March 2012. doi: 10.1103/physrevb.85.125124.

[35] H. L. Liu, K. S. Lu, M. X. Kuo, et al. Magneto-optical properties of $La_{0.7}Sr_{0.3}MnO_3$ thin films with perpendicular magnetic anisotropy. *Journal of Applied Physics*, 99(4):043908, February 2006. doi: 10.1063/1.2173681.

[36] S. Yamaguchi, Y. Okimoto, K. Ishibashi, and Y. Tokura. Magneto-optical kerr effects in perovskite-type transition-metal oxides: $La_xSr_{1-x}MnO_3$ and $La_xSr_{1-x}CoO_3$. *Physical Review B*, 58(11):6862–6870, September 1998. doi: 10.1103/physrevb.58.6862.

[37] F. Formisano, R. Medapalli, Y. Xiao, et al. Femtosecond magneto-optics of EuO. *Journal of Magnetism and Magnetic Materials*, 502:166479, May 2020. doi: 10.1016/j.jmmm.2020.166479.

[38] Z. Liao, R. Jin, E. W. Plummer, and J. Zhang. Delicate competing electronic states in ultrathin manganite films. *Physical Review B*, 95(8), feb 2017. doi: 10.1103/physrevb.95.085130.

List of Figures

List of Tables

List of Abbreviations

LSMO	-	$La_{2/3}Sr_{1/3}MnO_3$
STO	-	$SrTiO_3$
BTO	-	$BaTiO_3$
NS	-	nanosheet
LCP	-	left circular polarization
RCP	-	right circular polarization
CMR	-	colossal magnetoresistance
MO	-	magneto-optical
MOKE	-	magneto-optical Kerr effect
DE	-	double-exchange
PLD	-	pulsed laser deposition
AFM	-	atomic force microscopy
XRD	-	X-ray diffraction
VSM	-	vibrating-sample magnetometer
AC	-	alternating current
OOR	-	oxygen octahedra rotations
IR	-	infrared
UV	-	ultraviolet